IEEE Open Journal of
Industry Applications

Received 21 December 2020; revised 10 February 2021 and 4 March 2021; accepted 8 March 2021. Date of publication 15 March 2021; date of current version 2 April 2021. The review of this article was arranged by Associate Editor Petros Karamanakos.

Digital Object Identifier 10.1109/OJIA.2021.3066105

Model Predictive Control of Permanent Magnet Synchronous Motors in the Overmodulation Region Including Six-Step Operation

ANIAN BROSCH, OLIVER WALLSCHEID (Member, IEEE), AND JOACHIM BÖCKER (Senior Member, IEEE)

Department of Power Electronics and Electrical Drives, Paderborn University, 33098 Paderborn, Germany

CORRESPONDING AUTHOR: ANIAN BROSCH (e-mail: brosch@lea.upb.de)

This work was supported by the German Research Foundation (DFG) under the reference number BO 2535/20-1.

ABSTRACT This paper proposes a model predictive control scheme with a higher-level open-loop torque control and an underlying continuous-control-set model predictive current control (CCS-MPCC) combined with a space vector modulation and an integrated harmonic reference generator (HRG) for permanent magnet synchronous motors (PMSMs), which is able to utilize the DC-link voltage of a two-level inverter to its maximum during transient and steady-state conditions. By formulating the CCS-MPCC as a quadratic program with the voltage hexagon as inequality constraints, the MPCC's typical dynamic response can be achieved during transient operation. When the overmodulation region is reached, additional current harmonics are induced by the voltage constraints, causing a deterioration of the controller's performance. To overcome this problem a HRG is introduced, which calculates at each sampling instant a reference current that contains these harmonics by solving a boundary value problem, using an overmodulation method under the assumption of steady state.Hence, the HRG performs a model-based current reference trajectory prediction ensuring that the CCS-MPCC can enter the overmodulation region. This allows highest control dynamics even at the voltage constraint while ensuring a seamless transition from linear modulation to overmodulation and six-step operation. The method presented here is able to operate in the entire speed range including standstill. Thus, it is not necessary to switch between different controller frameworks for the constant-torque and constant-power regions. Extensive simulative and experimental investigations for a highly utilized PMSM with significant (cross-)saturation effects prove the viability of the proposed control methodology.

INDEX TERMS Continuous-control-set, flux weakening, model predictive control, overmodulation, permanent magnet synchronous motor, six-step operation.

I. INTRODUCTION

For advanced drive applications, permanent magnet synchronous motors (PMSMs) are the preferred choice if highest torque and power density is required. To achieve both, the drive system consisting of motor and inverter must be utilized to the highest possible extent. If the speed is below its nominal value, the motor operates in the constant-torque region. Here, the maximum torque depends only on the current limit. When the speed rises, the constant-power region is entered. In this region the maximum torque depends also on the voltage limit. For this reason it is crucial to utilize the DC-link voltage of the inverter to the maximum extent by increasing the modulation region towards overmodulation and the six-step operation. Only this way the torque and power density of the drive system can be maximized without any change of the hardware setup [1]–[3].

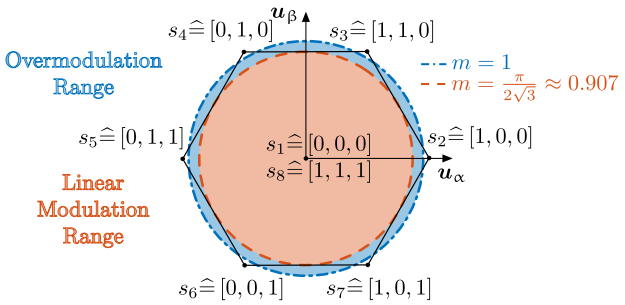

FIGURE 1. Linear modulation $0 \le m < \frac{\pi}{2\sqrt{3}}$ and overmodulation region $\frac{\pi}{2\sqrt{3}} < m \le 1$ in the $\alpha\beta$ coordinate system as well as the definition of the elementary vectors s_n with the corresponding switching positions of the inverter phases

A. STATE-OF-THE-ART TECHNIQUES

In the context of proportional-integral field orientated control (PI-FOC), the operating range can be extended to the constant-power region by adding a voltage controller that sets the reference point for the underlying current or torque controller [4]–[7]. To prevent the current controllers from saturation in the flux-weakening region, usually only the linear modulation region minus a voltage margin of about 5% is utilized by the range of the actuating variable. Characteristically, these current controllers are not able to operate continuously at the voltage limit, which leads to a suboptimal utilization of the inverter [5], [7].

To increase the modulation index beyond the linear modulation region the overmodulation region must be entered, blue-shaded area in Fig. 1. In this modulation region, additional torque and current harmonics are induced by the voltage constraints, causing a deterioration of the controller's performance or even instability of the closed control loop [8]. For PI-FOC, different approaches can be used to reduce this deterioration. In [9] low-pass current filters in the feedback path are used to suppress the current harmonics. However, this leads to a reduction of the controller bandwidth and system performance. Other methods use a machine model to estimate the current harmonics and to compensate for them within the control feedback loop [8], [10]–[12]. In [8] the harmonic machine model is used as an open-loop estimator. Here, the estimation in steady-state condition is accurate but will cause an instability problem in transient operation due to the difference of system poles [10]. To solve this problem, a feedback path was added to the estimator in [10]–[12], but nevertheless six-step operation was not achieved. In contrast, the method in [13] achieves six-step operation with a high-dynamic current control. Here, the reference voltage vector for the modulator rotates outside the voltage hexagon, ensuring six-step operation using Bolognani's overmodulation scheme [14]. The voltage vector rotates so far outside the voltage hexagon that the voltage corrections of the PI-FOC induced by the current harmonics of the six-step operation have no effect on the modulator. Instead in the overmodulation region in between the linear modulation region and the six-step operation the PI-FOC's actuating voltage vector would intersect the voltage hexagon. The excitation of the PI-FOC induced by the current harmonics would then lead to a deterioration and suboptimal control performance in this modulation region.

Compared to PI-FOC, especially when containing an anti-reset windup (ARW) scheme and operating nearby the voltage limit, the methods of model predictive control (MPC) are characterized by superior control dynamics. In addition to that, MPC methods can handle state and input constraints inherently and are therefore a promising control concept for the overmodulation region at the voltage limit [3], [15]–[22]. MPC methods can be divided into continuous-control-set (CCS) algorithms in combination with a modulator [20]–[22] and finite-control-set (FCS) methods that directly determine the switching pulses for the inverter [3], [15]–[19]. Despite the fact that the mentioned CCS-MPCC methods and the FCS-MPCC methods [16]–[19] increase the modulation index above the linear modulation region, they do not achieve six-step operation. However, in the context of FCS-MPCC, methods exist that can realize six-step operation [3], [15]. In [15] the inverter switching is sufficiently penalized in the FCS-MPCC cost function, such that six-step operation can be enforced. The proposed method in [3] in contrast, ensures the six-step operation by a special rectangular boundary area of the control error if it is desired.

In six-step operation, the fundamental voltage is maximum and the DC-link voltage of the inverter is completely utilized whereby the switching frequency is minimal. Extensive research on six-step operation has been conducted [2], [8], [13], [14], [23]–[30]. The contributions [14], [23]–[27] deal with the synthesis of voltage vectors in the overmodulation region and the six-step operation with the assumption of stationarity but not with closed-loop control dynamics. Depenbrock's direct self control (DSC) [28] or voltage angle controllers [2], [29], [30] are usually only applied in the constant-power region, whereby below the nominal speed in the constant-torque range a switchover to a current-based PI-FOC or another state-of-the-art controller is usually made. This switching between different control strategies can lead to transition shocks, which is not desirable especially for highly dynamic applications such as servo or automotive traction drives.

B. CONTRIBUTION

In order to overcome the problems mentioned above, this paper proposes a predictive control scheme, cf. Fig. 2, with the following elements:

- Higher-level open-loop torque controller that selects a current operating point based on the maximum-torque-per-current (MTPC) and maximum-torque-per-voltage (MTPV) strategies [31]–[33].
- Model-based harmonic reference generator (HRG) that adds harmonic components to the mean reference current, in which the effect of the inverter voltage limit is contained in case of overmodulation.
- CCS-MPCC that tracks the reference current supplied by the HRG.

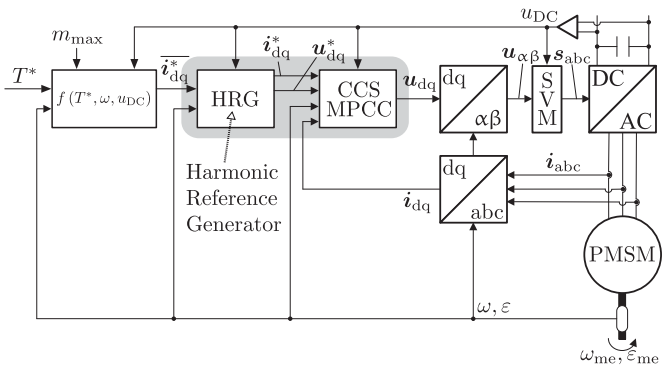

FIGURE 2. Overall model predictive control scheme with higher-level open-loop torque controller (gray-shaded part is focused within this paper)

- Space vector modulation (SVM) that converts the voltages commanded by the CCS-MPCC into switching commands for the inverter.

Thanks to the elements of the control scheme the following advantageous properties can be achieved:

- Loss optimal operating points are selected by the higher-level torque controller.
- The HRG enables a seamless transition within in the entire modulation range including six-step operation, which utilizes the DC-link voltage of the inverter to the maximum extent.
- Highest control dynamic is ensured by the CCS-MPCC even at the voltage limit.
- The control scheme is able to operate in the entire speed range including standstill, which makes it not necessary to switch between different controller frameworks for the constant-torque and constant-power regions.

Furthermore, it will be shown that the HRG can be also coupled with simple, linear proportional-integral feedback controllers within the field-oriented current control instead of a CCS-MPCC, which adds additional design alternatives to the proposed control scheme.

C. PAPER STRUCTURE

This paper is organized as follows. Section II describes the general control framework of the proposed approach. Section III focuses in detail on the HRG, whereby the solution of the BVP and its sensitivity to parameters and discretization methods are discussed. Section IV focuses on the simulative investigation of the presented method while also a digression on a possible combination of the HRG with a PI-FOC is considered. Additionally, extensive experimental investigations in the complete operating and modulation region are discussed in Section V. Finally, Section VI concludes this paper.

II. GENERAL CONTROL FRAMEWORK

In the following the overall control scheme shown in Fig. 2 is explained in more detail. In some situations or at some operating points the current and torque harmonics caused by overmodulation operation may be undesirable. For this reason, a maximum degree of modulation $m_{\max}$ can be provided as a parameter to the higher-level open-loop torque controller so that the selected operating points $\overline{\boldsymbol{i}^*_{\mathrm{dq}}}$ will not lead to an excess of this modulation index. However, $m_{\max} = 1$ applies for the remainder of this paper to fully utilize the DC-link voltage. It is further assumed that the fundamental current set points are chosen based on the usual MTPC and MTPV strategies [31], [32]. For this reason, the presented study concentrates on the underlying current control, which consists of the HRG and CCS-MPCC as depicted in Fig. 2. Given a mean current operating point $\overline{\boldsymbol{i}^*_{\mathrm{dq}}}$, a mean voltage vector can be calculated for steady-state operation using a precise motor model. On the basis of this mean voltage vector, a voltage trajectory $\boldsymbol{u}^*_{\mathrm{dq}}(t)$ leading to overmodulation (including six-step operation) can be calculated for stationary operation [24]. Using the harmonic voltage trajectory $\boldsymbol{u}^*_{\mathrm{dq}}(t)$, a numerical boundary value problem (BVP) for the calculation of the current trajectories $\boldsymbol{i}^*_{\mathrm{dq}}(t)$, i.e., the current trajectory incorporating a harmonic content with average value $\overline{\boldsymbol{i}^*_{\mathrm{dq}}}$, can be solved. This current trajectory contains the harmonics induced by the voltage constraints in the overmodulation scheme. The current reference value $\boldsymbol{i}^*_{\mathrm{dq}}[k]$ at the end of the sampling instant and the corresponding reference voltage $\boldsymbol{u}^*_{\mathrm{dq}}[k]$ are then supplied to an ordinary CCS-MPCC with a prediction horizon of $N = 1$. Here, a weighted sum of the quadratic control error and the voltage deviation $\boldsymbol{u}^*_{\mathrm{dq}}[k] - \boldsymbol{u}_{\mathrm{dq}}[k]$ is minimized with the voltage hexagon as a constraint. Penalizing the voltage deviation is necessary to ensure six-step operation, which is discussed in more detail in a separate section of the paper.

A. COORDINATE SYSTEMS

Transformations between stator-fixed three-phase *abc* and the stator-fixed $\alpha\beta$ coordinate system are calculated with the following matrices

$$\boldsymbol{T}_{\alpha\beta\mathrm{abc}} = \frac{2}{3}\begin{bmatrix} 1 & -\frac{1}{2} & -\frac{1}{2} \\ 0 & \frac{\sqrt{3}}{2} & -\frac{\sqrt{3}}{2} \end{bmatrix}, \quad \boldsymbol{T}_{\mathrm{abc}\alpha\beta} = \boldsymbol{T}^{\dagger}_{\alpha\beta\mathrm{abc}}. \tag{1}$$

Here, † denotes the Moore-Penrose pseudoinverse and bold symbols depict matrices/vectors. Transformations between the $\alpha\beta$ and rotor-fixed *dq* coordinate system are formulated in a similar way

$$\begin{aligned} \boldsymbol{T}_{\mathrm{dq}\alpha\beta}(\varepsilon) &= \begin{bmatrix} \cos(\varepsilon) & \sin(\varepsilon) \\ -\sin(\varepsilon) & \cos(\varepsilon) \end{bmatrix}, \\ \boldsymbol{T}_{\alpha\beta\mathrm{dq}}(\varepsilon) &= \boldsymbol{T}^{-1}_{\mathrm{dq}\alpha\beta}(\varepsilon). \end{aligned} \tag{2}$$

Above, ε denotes the electrical rotation angle of the PMSM. With the help of (1) and (2) the transformations between the *abc* and *dq* coordinate system can be obtained

$$\begin{aligned} \boldsymbol{T}_{\mathrm{dqabc}}(\varepsilon) &= \boldsymbol{T}_{\mathrm{dq}\alpha\beta}(\varepsilon)\boldsymbol{T}_{\alpha\beta\mathrm{abc}}, \\ \boldsymbol{T}_{\mathrm{abcdq}}(\varepsilon) &= \boldsymbol{T}^{\dagger}_{\mathrm{dqabc}}(\varepsilon). \end{aligned} \tag{3}$$

B. DISCRETE-TIME PMSM WHITE-BOX MODEL

The discrete-time current difference equation of a PMSM considering (cross-)saturation effects in the dq coordinate system can be described as follows [34]

$$\boldsymbol{i}_{\mathrm{dq}}[k+1] = \boldsymbol{A}_{\mathrm{d}}\big(\boldsymbol{i}_{\mathrm{dq}}[k]\big)\boldsymbol{i}_{\mathrm{dq}}[k] + \boldsymbol{B}_{\mathrm{d}}\big(\boldsymbol{i}_{\mathrm{dq}}[k]\big)\boldsymbol{u}_{\mathrm{dq}}[k] + \boldsymbol{E}_{\mathrm{d}}\big(\boldsymbol{i}_{\mathrm{dq}}[k]\big)$$

with:

$$\begin{aligned}
\boldsymbol{A}_{\mathrm{d}}\big(\boldsymbol{i}_{\mathrm{dq}}[k]\big) &= \boldsymbol{I}_2 - \boldsymbol{L}^{-1}_{\mathrm{dq},\Delta}\big(\boldsymbol{i}_{\mathrm{dq}}[k]\big)R_{\mathrm{s}}\mathrm{T_s},\\
\boldsymbol{B}_{\mathrm{d}}\big(\boldsymbol{i}_{\mathrm{dq}}[k]\big) &= \boldsymbol{L}^{-1}_{\mathrm{dq},\Delta}\big(\boldsymbol{i}_{\mathrm{dq}}[k]\big)\boldsymbol{T}_{\alpha\beta\mathrm{dq}}(-\mathrm{T_s}\omega)\mathrm{T_s},\\
\boldsymbol{E}_{\mathrm{d}}\big(\boldsymbol{i}_{\mathrm{dq}}[k]\big) &= \boldsymbol{L}^{-1}_{\mathrm{dq},\Delta}\big(\boldsymbol{i}_{\mathrm{dq}}[k]\big)\left[\boldsymbol{T}_{\alpha\beta\mathrm{dq}}(-\mathrm{T_s}\omega) - \boldsymbol{I}_2\right]\boldsymbol{\psi}_{\mathrm{dq}}\big(\boldsymbol{i}_{\mathrm{dq}}[k]\big).
\end{aligned} \tag{4}$$

Here, $\boldsymbol{i}_{\mathrm{dq}} = [i_{\mathrm{d}} \quad i_{\mathrm{q}}]^{\mathrm{T}}$ represents the stator current, $\boldsymbol{\psi}_{\mathrm{dq}}(\boldsymbol{i}_{\mathrm{dq}}) = [\psi_{\mathrm{d}}(\boldsymbol{i}_{\mathrm{dq}}) \quad \psi_{\mathrm{q}}(\boldsymbol{i}_{\mathrm{dq}})]^{\mathrm{T}}$ the flux linkage, $\boldsymbol{u}_{\mathrm{dq}} = [u_{\mathrm{d}} \quad u_{\mathrm{q}}]^{\mathrm{T}}$ the stator voltage, R_{s} the stator resistance, ω the electrical angular velocity, $\mathrm{T_s}$ the sampling time, $\boldsymbol{I}_2$ the identity matrix and $\boldsymbol{L}_{\mathrm{dq},\Delta}$ the differential inductance matrix defined by

$$\boldsymbol{L}_{\mathrm{dq},\Delta}\big(\boldsymbol{i}_{\mathrm{dq}}\big) = \begin{bmatrix} L_{\mathrm{dd}}\big(\boldsymbol{i}_{\mathrm{dq}}\big) & L_{\mathrm{dq}}\big(\boldsymbol{i}_{\mathrm{dq}}\big) \\ L_{\mathrm{qd}}\big(\boldsymbol{i}_{\mathrm{dq}}\big) & L_{\mathrm{qq}}\big(\boldsymbol{i}_{\mathrm{dq}}\big) \end{bmatrix} = \begin{bmatrix} \frac{\partial\psi_{\mathrm{d}}}{\partial i_{\mathrm{d}}} & \frac{\partial\psi_{\mathrm{d}}}{\partial i_{\mathrm{q}}} \\ \frac{\partial\psi_{\mathrm{q}}}{\partial i_{\mathrm{d}}} & \frac{\partial\psi_{\mathrm{q}}}{\partial i_{\mathrm{q}}} \end{bmatrix}. \tag{5}$$

For ease of reading, the speed dependency of the system matrices $\boldsymbol{A}_{\mathrm{d}}$, $\boldsymbol{B}_{\mathrm{d}}$, $\boldsymbol{E}_{\mathrm{d}}$ is dropped. The term $\boldsymbol{T}_{\alpha\beta\mathrm{dq}}(-\mathrm{T_s}\omega)$ considers the rotation of the dq against the $\alpha\beta$ coordinate system during a sampling period [35], [36].

C. CONTINUOUS-CONTROL-SET MODEL PREDICTIVE CURRENT CONTROL

The cost function for the CCS-MPCC with a prediction horizon of $N = 1$ is designed to penalize the weighted squared Euclidean distance from the predicted current $\boldsymbol{i}_{\mathrm{dq}}[k+1]$ to the reference current at the next time step $\boldsymbol{i}^*_{\mathrm{dq}}[k+1]$. In the same way the difference between the voltage $\boldsymbol{u}_{\mathrm{dq}}[k]$, which is needed to attain the current $\boldsymbol{i}^*_{\mathrm{dq}}[k+1]$ and a given reference voltage $\boldsymbol{u}^*_{\mathrm{dq}}[k]$ is penalized. This penalization can be used to realize six-step operation, which is discussed in more detail in Sec. III-F. The optimization problem can thus be defined as

$$\min_{\boldsymbol{u}_{\mathrm{dq}}[k]} \quad \|\boldsymbol{i}_{\mathrm{dq}}[k+1] - \boldsymbol{i}^*_{\mathrm{dq}}[k+1]\|^2_{\boldsymbol{Q}} + \|\boldsymbol{u}_{\mathrm{dq}}[k] - \boldsymbol{u}^*_{\mathrm{dq}}[k]\|^2_{\boldsymbol{R}} \tag{6a}$$

$$\text{s.t.} \quad \boldsymbol{u}_{\mathrm{dq}}[k] \in \mathcal{U}_{\mathrm{dq}}, \tag{6b}$$

$$\begin{aligned}
\boldsymbol{i}_{\mathrm{dq}}[k+1] = {} & \boldsymbol{A}_{\mathrm{d}}\big(\boldsymbol{i}_{\mathrm{dq}}[k]\big)\boldsymbol{i}_{\mathrm{dq}}[k] \\
& + \boldsymbol{B}_{\mathrm{d}}\big(\boldsymbol{i}_{\mathrm{dq}}[k]\big)\boldsymbol{u}_{\mathrm{dq}}[k] \\
& + \boldsymbol{E}_{\mathrm{d}}\big(\boldsymbol{i}_{\mathrm{dq}}[k]\big).
\end{aligned} \tag{6c}$$

Here, the set $\mathcal{U}_{\mathrm{dq}}$ is defined as

$$\boldsymbol{u}_{\mathrm{dq}} \in \mathcal{U}_{\mathrm{dq}} = \left\{\boldsymbol{u}_{\mathrm{dq}} \in \mathbb{R}^2 | \boldsymbol{u}_{\mathrm{dq}} = u_{\mathrm{DC}}\boldsymbol{T}_{\mathrm{dqabc}}\boldsymbol{d}_{\mathrm{abc}}\right\} \tag{7}$$

where u_{DC} is the DC-link voltage and $\boldsymbol{d}_{\mathrm{abc}}$ is the duty cycle vector of the inverter given by

$$\boldsymbol{d}_{\mathrm{abc}} = \begin{bmatrix} d_{\mathrm{a}} & d_{\mathrm{b}} & d_{\mathrm{c}} \end{bmatrix}^{\mathrm{T}} \in [0,1]^3 \subset \mathbb{R}^3. \tag{8}$$

To solve the linearly constrained quadratic program (LCQP) (6), any standard quadratic programming (QP) solver can be utilized. For the practical implementation of this contribution, the embedded solver of the Matlab MPC toolbox was chosen [37], [38]. To compensate for the control delay due to the digital implementation a one-step state prediction is applied before the QP solver is called [39].

D. OVERMODULATION SCHEME

As mentioned in Sec. I-B, the proposed HRG uses voltage trajectories and a motor model to calculate the reference current trajectories in the overmodulation region by solving a numerical BVP with the help of matrix inversion. With a given fundamental voltage vector in the dq coordinate system and the modulation index, a overmodulation scheme is able to synthesize these voltage trajectories for a sixth of the fundamental wave. To utilize the entire modulation region an overmodulation method must be applied, which also covers the six-step operation. Here, a few of these can be mentioned [14], [24]–[26]. In this paper, Holtz's method [24] was utilized because of its low harmonic distortion [27]. For readers who are not experienced with any of the previously mentioned overmodulation techniques [14], [24]–[26], the proposed control framework in this paper will be easier to understand if they are familiarized with the overmodulation schemes beforehand.

III. HARMONIC REFERENCE GENERATOR

As mentioned in the previous section, the additional current harmonics induced by the voltage constraints lead to a deterioration of the performance of conventional current controllers. In this paper instead, the deterioration of the performance of the current controller is prevented by the HRG, which is the core of this work, by calculating these current harmonics using voltage trajectories and solving a numerical BVP. The calculated current harmonics and voltage trajectories are then used as a model-based feed-forward reference compensation. This results in the fact that the occurring current harmonics in the feedback path of the current control loop no longer deteriorate the performance of the controller. For this reason, the calculation steps and methodology of the HRG are described in the following. At first, the concept is explained for PMSMs without significant (cross-)saturation, in the remainder of this paper referred to aslinear-magnetized (LM-)PMSMs. In a second step, the (cross-)saturation of PMSMs is also taken into account, referred to as nonlinear-magnetized (NM-)PMSMs followed by an accuracy investigation of the presented method. A flowchart of the entire HRG algorithm is shown in Fig. 3.

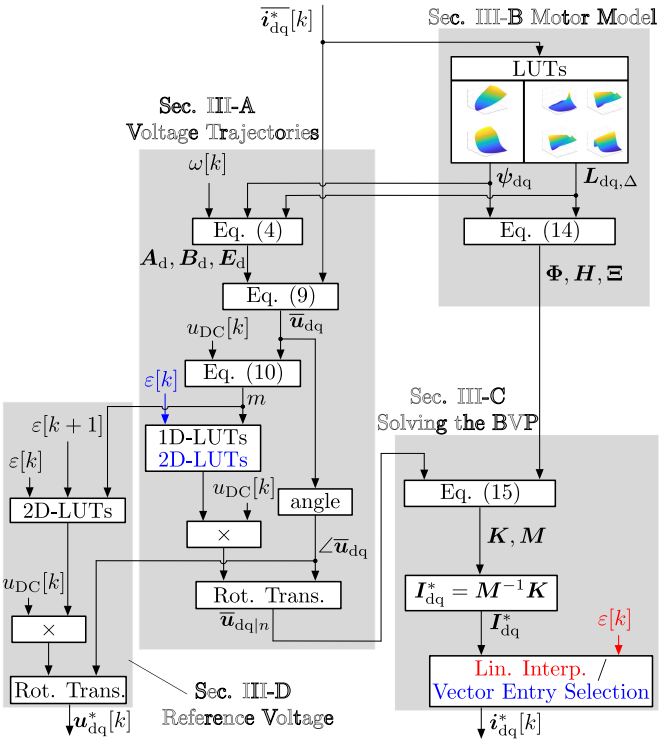

FIGURE 3. Flow chart of the HRG for the LI method (red) and the VSP method (blue)

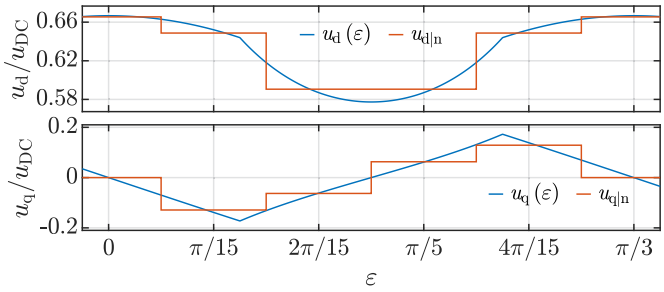

FIGURE 4. Continuous (blue) and discretized (red) voltage trajectories ($N_{BP} = 5$) for an angle of $\angle\overline{u}_{dq} = 0$ and a modulation index of $m = 0.988$

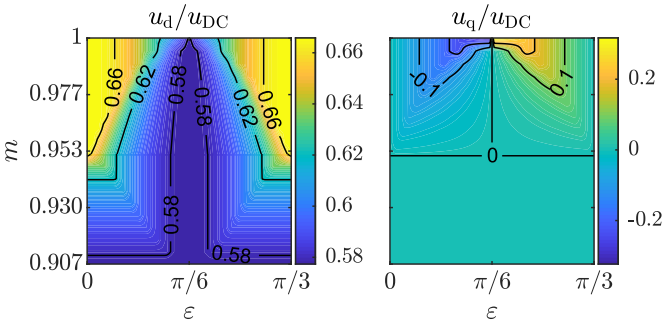

FIGURE 5. Continuous voltage values as a function of the modulation index m and the electrical rotation angle ε for an angle of $\angle\overline{u}_{dq} = 0$

A. VOLTAGE TRAJECTORIES

At the beginning of each sampling interval the fundamental current reference $\overline{i^*_{dq}}$ is provided to the HRG by the higher-level torque control, see Fig. 2. With the speed ω and motor parameters the system matrices $\boldsymbol{A}_d$, $\boldsymbol{B}_d$, $\boldsymbol{E}_d$ can be calculated. The steady-state fundamental voltage vector can be calculated as follows

$$\overline{\boldsymbol{u}}_{dq} = \boldsymbol{B}_d^{-1}\left(\boldsymbol{i}_{dq}[k]\right)\left(\left(\boldsymbol{I}_2 - \boldsymbol{A}_d\left(\boldsymbol{i}_{dq}[k]\right)\right)\overline{\boldsymbol{i}^*_{dq}} - \boldsymbol{E}_d\left(\boldsymbol{i}_{dq}[k]\right)\right). \tag{9}$$

The modulation index, which is in the range from zero to one, is defined as

$$m = \frac{|\overline{\boldsymbol{u}}_{dq}|}{\frac{2}{\pi}u_{DC}}. \tag{10}$$

When the modulation index is in the linear modulation region $|\overline{\boldsymbol{u}}_{dq}| \leq u_{DC}/\sqrt{3}$, no further calculations have to be performed by the HRG and the current reference for the CCS-MPCC is set to $\boldsymbol{i}^*_{dq} = \overline{\boldsymbol{i}^*_{dq}}$.

In the following, operation within the overmodulation region is assumed. With the modulation index and the angle $\angle\overline{\boldsymbol{u}}_{dq}$, the voltage trajectories over a sixth of the fundamental period can now be calculated with the help of an overmodulation scheme [24] in the dq coordinate system. In Fig. 4 an exemplary continuous voltage trajectory $\boldsymbol{u}_{dq}(\varepsilon)$ is depicted.Fig. 5 contains the continuous electrical rotation angle dependend voltage trajectories as a function of the modulation index for an angle of $\angle\overline{\boldsymbol{u}}_{dq} = 0$ and can therefore be seen as an extension of Fig. 4. Even if the values of Fig. 5 are valid only for $\angle\overline{\boldsymbol{u}}_{dq} = 0$, the voltage trajectories, and therefore the behavior of the applied overmodulation scheme [24], will be defined uniquely with Fig. 5 since the voltage values for any angle $\angle\overline{\boldsymbol{u}}_{dq}$ can be calculated by a simple rotary transformation for the desired angle $\angle\overline{\boldsymbol{u}}_{dq}$. Furthermore, the dual-mode property of the applied overmodulation scheme [24] can be seen in Fig. 5, because up to a modulation index of $m = 0.952$ the voltage vector $\boldsymbol{u}_{dq}$ is in phase with the mean voltage vector $\overline{\boldsymbol{u}}_{dq}$, resulting in $u_d = 0$ for $\angle\overline{\boldsymbol{u}}_{dq} = 0$.

With the help of the voltage trajectories the current trajectories are calculated numerically by solving a BVP. Here, the current trajectory is calculated at N_{BP} equidistant distributed supporting points, also referred to as mesh oder grid points [40], over the interval $\pi/3$. For this reason the continuous voltage trajectories must be discretized into N_{BP} sections, see Fig. 4. The calculation of the continuous voltage trajectories followed by a discretization is very computationally intensive during online operation. For this reason it is more efficient to store the voltage values for each supporting point as a function of the modulation index in an one-dimensional look-up table (LUT) offline for $\angle\overline{\boldsymbol{u}}_{dq} = 0$ and then transform them online to the actual angle $\angle\overline{\boldsymbol{u}}_{dq}$ using a rotary transformation. It should be noted that this pre-calculation is fully independent of the specific drive design (motor & inverter ratings) and, therefore, does not limit the scope of the proposed solution approach.

B. MOTOR MODEL

For the solution of the BVP a different motor model than (4) is applied for two reasons. Firstly, the rotation of dq against the $\alpha\beta$ coordinate system during a transition from one supporting point to the next can be taken into account by the discretized voltage trajectories stored in the LUTs, and, therefore this rotation does not have to be compensated by the motor model. Secondly, the model (4) will only be valid if the present current point $\boldsymbol{i}_{\mathrm{dq}}[k]$ is identical to the current point, at which the flux and differential inductance values are determined, because the flux is treated as a constant. This will not be a problem if the current point, at which the model has to be evaluated, is known, e.g. for the CCS-MPCC from Sec. II-C. However, for the BVP, the current trajectories are not known a priori, only the mean reference current $\overline{\boldsymbol{i}^*_{\mathrm{dq}}}$. For this reason the model coverage has to be increased in the proximity of this point. Starting from the ordinary differential equation (ODE) of an LM-PMSM

$$\frac{\mathrm{d}\boldsymbol{i}_{\mathrm{dq}}(t)}{\mathrm{d}t} = \boldsymbol{L}^{-1}_{\mathrm{dq},\Delta}\left(-R_{\mathrm{s}}\boldsymbol{i}_{\mathrm{dq}}(t) + \boldsymbol{u}_{\mathrm{dq}}(t) - \omega\boldsymbol{J}\boldsymbol{\psi}_{\mathrm{dq}}(t)\right) \tag{11}$$

with the 90°-rotation matrix $\boldsymbol{J}$, the model coverage can be increased for the NM-PMSM case by inserting the linearized flux linkage equation around $\overline{\boldsymbol{i}^*_{\mathrm{dq}}}$

$$\boldsymbol{\psi}_{\mathrm{dq}}\left(\boldsymbol{i}_{\mathrm{dq}}\right) \approx \boldsymbol{\psi}_{\mathrm{dq}}\left(\overline{\boldsymbol{i}^*_{\mathrm{dq}}}\right) + \boldsymbol{L}_{\mathrm{dq},\Delta}\left(\overline{\boldsymbol{i}^*_{\mathrm{dq}}}\right)\left[\boldsymbol{i}_{\mathrm{dq}} - \overline{\boldsymbol{i}^*_{\mathrm{dq}}}\right], \tag{12}$$

in (11) which will result in the following continuous-time NM-system

$$\begin{aligned}
\frac{\mathrm{d}\boldsymbol{i}_{\mathrm{dq}}(t)}{\mathrm{d}t} &= \boldsymbol{A}\left(\overline{\boldsymbol{i}^*_{\mathrm{dq}}}\right)\boldsymbol{i}_{\mathrm{dq}}(t) + \boldsymbol{B}\left(\overline{\boldsymbol{i}^*_{\mathrm{dq}}}\right)\boldsymbol{u}_{\mathrm{dq}}(t) + \boldsymbol{E}\left(\overline{\boldsymbol{i}^*_{\mathrm{dq}}}\right)\\
&\text{with:}\\
\boldsymbol{A}\left(\overline{\boldsymbol{i}^*_{\mathrm{dq}}}\right) &= -\boldsymbol{L}^{-1}_{\mathrm{dq},\Delta}\left(\overline{\boldsymbol{i}^*_{\mathrm{dq}}}\right)\left[\boldsymbol{I}_2 R_{\mathrm{s}} + \omega\boldsymbol{J}\boldsymbol{L}_{\mathrm{dq},\Delta}\left(\overline{\boldsymbol{i}^*_{\mathrm{dq}}}\right)\right],\\
\boldsymbol{B}\left(\overline{\boldsymbol{i}^*_{\mathrm{dq}}}\right) &= \boldsymbol{L}^{-1}_{\mathrm{dq},\Delta}\left(\overline{\boldsymbol{i}^*_{\mathrm{dq}}}\right),\\
\boldsymbol{E}\left(\overline{\boldsymbol{i}^*_{\mathrm{dq}}}\right) &= -\omega\boldsymbol{L}^{-1}_{\mathrm{dq},\Delta}\left(\overline{\boldsymbol{i}^*_{\mathrm{dq}}}\right)\boldsymbol{J}\left[\boldsymbol{\psi}_{\mathrm{dq}}\left(\overline{\boldsymbol{i}^*_{\mathrm{dq}}}\right) - \boldsymbol{L}_{\mathrm{dq},\Delta}\left(\overline{\boldsymbol{i}^*_{\mathrm{dq}}}\right)\overline{\boldsymbol{i}^*_{\mathrm{dq}}}\right].
\end{aligned} \tag{13}$$

After the continuous-time model (13) has been constructed with the help of LUTs for the differential inductances and flux linkages, a discrete-time model must be derived with the time $\mathrm{T_a} = \frac{\pi}{3\omega N_{\mathrm{BP}}}$ between two supporting points as discretization step size. Here, for example, the exact discretization (ED) or the forward Euler (FE) method as a typical approximation can be used

$$\begin{aligned}
\boldsymbol{i}_{\mathrm{dq}}[n+1] &= \boldsymbol{\Phi}\left(\overline{\boldsymbol{i}^*_{\mathrm{dq}}}\right)\boldsymbol{i}_{\mathrm{dq}}[n] + \boldsymbol{H}\left(\overline{\boldsymbol{i}^*_{\mathrm{dq}}}\right)\boldsymbol{u}_{\mathrm{dq}}[n] + \boldsymbol{\Xi}\left(\overline{\boldsymbol{i}^*_{\mathrm{dq}}}\right)\\
&\text{with:}\\
\boldsymbol{\Phi}\left(\overline{\boldsymbol{i}^*_{\mathrm{dq}}}\right) &= e^{\boldsymbol{A}\mathrm{T_a}} \approx \boldsymbol{I}_2 + \boldsymbol{A}\mathrm{T_a},\\
\boldsymbol{H}\left(\overline{\boldsymbol{i}^*_{\mathrm{dq}}}\right) &= \boldsymbol{A}^{-1}\left(e^{\boldsymbol{A}\mathrm{T_a}} - \boldsymbol{I}_2\right)\boldsymbol{B} \approx \mathrm{T_a}\boldsymbol{B},\\
\boldsymbol{\Xi}\left(\overline{\boldsymbol{i}^*_{\mathrm{dq}}}\right) &= \boldsymbol{A}^{-1}\left(e^{\boldsymbol{A}\mathrm{T_a}} - \boldsymbol{I}_2\right)\boldsymbol{E} \approx \mathrm{T_a}\boldsymbol{E}.
\end{aligned} \tag{14}$$

C. SOLVING THE BOUNDARY VALUE PROBLEM

Using (14), the discretized voltages $\boldsymbol{u}_{\mathrm{dq|n}}$ and assuming the periodicity of the reference current trajectories, the following linear equation system can be constructed

$$\underbrace{\begin{bmatrix}
\boldsymbol{\Xi} + \boldsymbol{H}\boldsymbol{u}_{\mathrm{dq}|1}\\
\boldsymbol{\Xi} + \boldsymbol{H}\boldsymbol{u}_{\mathrm{dq}|2}\\
\vdots\\
\boldsymbol{\Xi} + \boldsymbol{H}\boldsymbol{u}_{\mathrm{dq}|N_{\mathrm{BP}}-1}\\
\boldsymbol{\Xi} + \boldsymbol{H}\boldsymbol{u}_{\mathrm{dq}|N_{\mathrm{BP}}}
\end{bmatrix}}_{\boldsymbol{K}}
= \underbrace{\begin{bmatrix}
-\boldsymbol{\Phi} & \boldsymbol{I}_2 & 0 & \dots & 0 & 0\\
0 & -\boldsymbol{\Phi} & \boldsymbol{I}_2 & \dots & 0 & 0\\
\vdots & \vdots & \vdots & \ddots & \vdots & \vdots\\
0 & 0 & 0 & \dots & -\boldsymbol{\Phi} & \boldsymbol{I}_2\\
\boldsymbol{I}_2 & 0 & 0 & \dots & 0 & -\boldsymbol{\Phi}
\end{bmatrix}}_{\boldsymbol{M}}
\underbrace{\begin{bmatrix}
\boldsymbol{i}^*_{\mathrm{dq}|1}\\
\boldsymbol{i}^*_{\mathrm{dq}|2}\\
\vdots\\
\boldsymbol{i}^*_{\mathrm{dq}|N_{\mathrm{BP}}-1}\\
\boldsymbol{i}^*_{\mathrm{dq}|N_{\mathrm{BP}}}
\end{bmatrix}}_{\boldsymbol{I}^*_{\mathrm{dq}}} \tag{15}$$

with the known sparse block matrix $\boldsymbol{M}$ and the vector $\boldsymbol{K}$ as well as the unknown vector $\boldsymbol{I}^*_{\mathrm{dq}}$ containing the supporting points of the current trajectories. By inverting $\boldsymbol{M}$ the solution vector $\boldsymbol{I}^*_{\mathrm{dq}}$ can be determined

$$\boldsymbol{I}^*_{\mathrm{dq}} = \boldsymbol{M}^{-1}\boldsymbol{K}. \tag{16}$$

The reference current for the CCS-MPCC at a certain control cycle can then be easily obtained by linear interpolation of the solution vector at $(\varepsilon[k] + \omega[k]\mathrm{T_s}) \pmod{\pi/3}$, in the remainder of this paper referred to as *linear interpolation* (LI) method. To gain a deeper understanding of the accuracy of the solution of the BVP, the current reference trajectories based on the LI method for $N_{\mathrm{BP}} = 3$ were compared against the analytical solution, see Fig. 6. Here, the six-step operation at an operation point of $\overline{\boldsymbol{i}^*_{\mathrm{dq}}} = \begin{bmatrix}-200\mathrm{A} & 150\mathrm{A}\end{bmatrix}^{\mathrm{T}}$ is applied because an analytic solution can be easily determined there. The parameters of the utilized LM-PMSM model are given in Table 1.

In Fig. 6 it can be seen that significant errors are made between some supporting points with the LI method. One way to circumvent this problem would be to increase the number

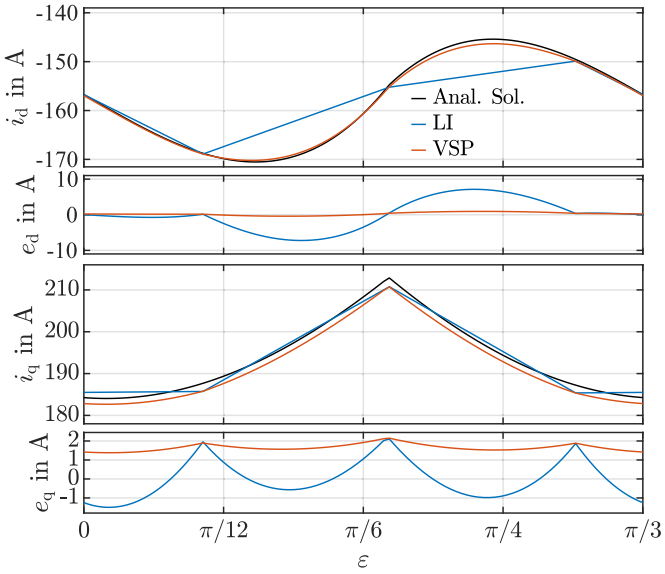

FIGURE 6. Current reference and error trajectories $e_{d,q}(\varepsilon)$ obtained by the LI and VSP method for $N_{BP} = 3$, $m = 1$ using ED as discretization method

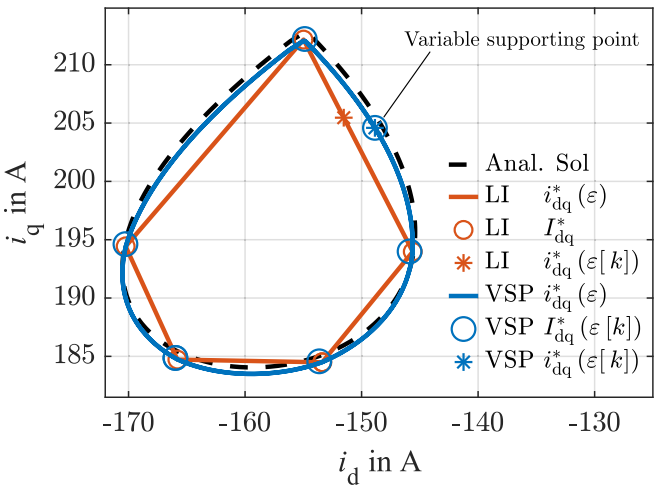

FIGURE 7. Analytic solution and numerical solution vector I^*_{dq}, exemplary reference current $i^*_{dq}(\varepsilon[k])$ for a specific electrical angle $\varepsilon[k]$, as well as the resulting reference current trajectories $i^*_{dq}(\varepsilon)$ obtained by the LI and VSP method for $N_{BP} = 5$ supporting points at a modulation index $m = 1$ using ED as discretization method

TABLE 1. LM-PMSM Model Parameters

DC-link voltage	u_{DC}	300 V
Nominal torque	T_{nom}	172 Nm
Nominal current	I	177 A
Stator resistance	R_s	18 mΩ
Permanent magnet flux	ψ_p	68 mVs
Inductances	L_d	0.37 mH
	L_q	1.2 mH

of supporting points. However, this increases the dimension of the matrix $\boldsymbol{M}$ that has to be inverted, which could affect the real-time capability of the algorithm. For this reason, a further method is proposed called *variable supporting point* (VSP) method.

The VSP method is based on the fact that the accuracy of the solution trajectories is only of interest at the angle $(\varepsilon[k] + \omega[k]T_s) \pmod{\pi/3}$ and not over the complete angular range. For this reason an additional supporting point is added at the specific angle, which results in an additional row in the linear equation system (15). The resulting reference trajectory of the VSP method is also depicted in Fig. 6. The VSP method is further explained in more detail using Fig. 7. Here, the entries of the solution vector $\boldsymbol{I}^*_{dq}$ for the LI method are depicted. For the LI method the solution vector does not depend on the electrical rotation angle $\varepsilon[k]$ of the PMSM. The reference current for the desired angle $\varepsilon[k]$ is then calculated by a linear interpolation of the solution vector, whereby an exemplary reference current $\boldsymbol{i}^*_{dq}(\varepsilon[k])$ is shown. Due to the linear interpolation, the trajectory of the reference current $\boldsymbol{i}^*_{dq}(\varepsilon)$ is given by the connection lines between the entries of the solution vector. In contrast to the LI method, the solution vector of the VSP method depends on the rotation angle because an additional supporting point is inserted at the rotation angle of interest. A solution vector $\boldsymbol{I}^*_{dq}([k])$ and the corresponding reference value $\boldsymbol{i}^*_{dq}(\varepsilon[k])$ at the current angle of interest $\varepsilon[k]$ is shown as well. By varying the rotation angle of interest from 0 to $\pi/6$, the reference trajectories $\boldsymbol{i}^*_{dq}(\varepsilon)$ for the LI and VSP method result. Here, it can be seen that the reference trajectory for the VSP method achieves a higher accuracy than the LI method compared to the analytical solution, see Fig. 7.

However, the VSP has a disadvantage compared to the LI method, which can be compensated in a computationally time-efficient way, as it will be shown in the following. For the LI method and a fixed number of supporting points N_{BP}, the angle between two supporting points is constant, allowing a discretization of the voltage trajectories to be performed offline. The discretized voltage trajectories can thus be stored in N_{BP} 1D-LUTs as a function of the modulation index, allowing a computationally time-efficient read-out during online operation. Because of the variable supporting point of the VSP method not all angles between the supporting points are constant, namely the neighboring angle differences of the variable supporting point. For this reason, the two neighboring entries $\boldsymbol{u}_{dq|n}$ of the variable supporting point of the vector $\boldsymbol{K}$ must be discretized online from the time-continuous voltage trajectories of Fig. 5 by averaging

$$u_{d,q|n} = \frac{1}{\varepsilon_{n+1} - \varepsilon_n} \int_{\varepsilon_n}^{\varepsilon_{n+1}} u_{d,q}(\tilde{\varepsilon}) \mathrm{d}\tilde{\varepsilon}, \tag{17}$$

$$= \frac{1}{\varepsilon_{n+1} - \varepsilon_n} \left(\int_0^{\varepsilon_{n+1}} u_{d,q}(\tilde{\varepsilon}) \mathrm{d}\tilde{\varepsilon} - \int_0^{\varepsilon_n} u_{d,q}(\tilde{\varepsilon}) \mathrm{d}\tilde{\varepsilon} \right). \tag{18}$$

Since the numerical solution of (17) requires an increased number of evaluations of a 2D-LUT containing the voltage maps from Fig. 5, this results in increased computation time. For this reason, not the voltage maps from Fig. 5 are stored in 2D-LUTs, but their integrals over the electrical angle from Fig. 8. This allows the averaging between two angles to be

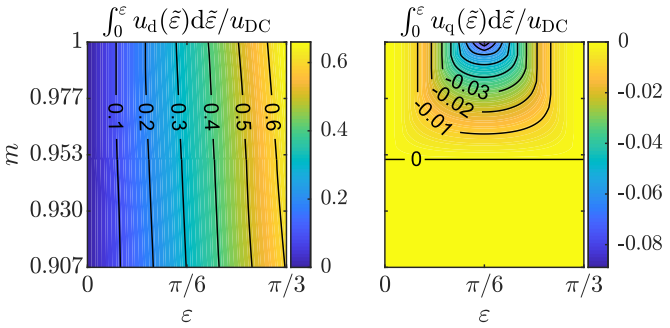

FIGURE 8. Integral of the modulation index-dependent voltage trajectories of Fig. 5 over the electrical rotation angle

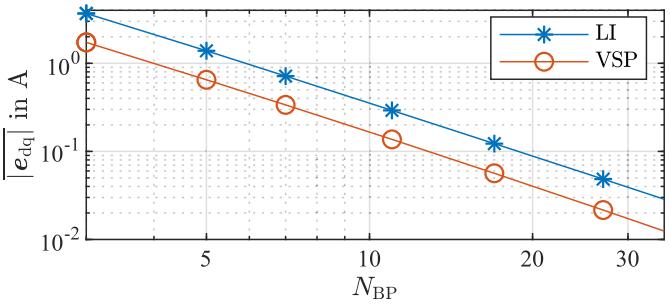

FIGURE 9. Mean error of the LI and VSP method for $m = 1$ at $\overline{i^*_\mathrm{dq}} = [-158 \quad 194]^\mathrm{T}$A using ED as discretization method

calculated with the help of (18) using two evaluations of the 2D-LUTs. This reduces the computation time during online operation.

To investigate the influence of the number of supporting points on the accuracy, the mean error of both methods compared to the analytic solution is shown in Fig. 9. The mean error is defined as

$$\overline{|\boldsymbol{e}_\mathrm{dq}|} = \frac{6}{\pi}\int_0^{\pi/6}\sqrt{{e_\mathrm{d}}^2(\varepsilon)+{e_\mathrm{q}}^2(\varepsilon)}\mathrm{d}\varepsilon. \tag{19}$$

In Fig. 9, it can be seen that the mean error decreases exponentially with the number of supporting points and the VSP method approximately halves the error compared to the LI method. For this reason, only the VSP method is applied in the remainder of this paper. So far only six-step operation was examined because here the solution can be verified by comparison to the analytical solution of the problem. For this reason, the reference current trajectories determined with the VSP method for different modulation indices are shown in Fig. 10.

D. REFERENCE VOLTAGE

In the context of optimal controllers, e.g. the linear-quadratic regulator (LQR) or the utilized CCS-MPCC, additional terms in the cost function can be used to penalize the deviation of the input to a reference input. For this reason, the reference voltage $\boldsymbol{u}^*_\mathrm{dq}[k]$ must be provided by the HRG to the current controller. On the one hand, in the linear modulation region the reference voltage can be computed via (9) and results to

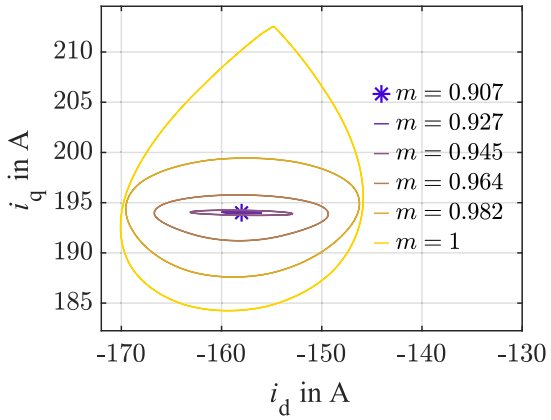

FIGURE 10. Exemplary reference current trajectories in the overmodulation regionobtained by the VSP method for different modulation indices with $N_\mathrm{BP} = 9$ using ED as discretization method (please note that $m = 0.907$ defines the end of the linear modulation region)

$\boldsymbol{u}^*_\mathrm{dq}[k] = \overline{\boldsymbol{u}}_\mathrm{dq}[k]$. In the overmodulation region, on the other hand, the phase and amplitude of the reference voltage $\boldsymbol{u}^*_\mathrm{dq}[k]$ varies even for a constant $\overline{\boldsymbol{u}}_\mathrm{dq}[k]$ due to the voltage constraint. The reference voltage can be calculated by applying the utilized overmodulation scheme to the average voltage vector $\overline{\boldsymbol{u}}_\mathrm{dq}[k]$ and the momentary motor angle $\varepsilon[k]$. Alternatively, the average reference voltage between the momentary electric rotor angle $\varepsilon[k]$ and the electric rotor angle $\varepsilon[k+1] = \varepsilon[k] + \omega \mathrm{T_s}$ of the next sampling step can be calculated. This leads to a higher accuracy at high speeds ω where a large angle difference $\omega \mathrm{T_s}$ per sampling step is passed. The calculation process can be seen in Fig. 3. Here, the reference voltage for $\angle\overline{\boldsymbol{u}}_\mathrm{dq} = 0$ is calculated with (18), the modulation index $m[k]$, the electrical rotor angles $\varepsilon[k]$, $\varepsilon[k+1]$, and the 2D-LUTs, which contain the maps of Fig. 8. Finally, the reference voltage $\boldsymbol{u}^*_\mathrm{dq}[k]$ must be rotated with the actual angle $\angle\overline{\boldsymbol{u}}_\mathrm{dq}[k]$ using a rotary transformation.

E. PARAMETERAND DISCRETIZATION ACCURACY INVESTIGATION

As shown in the previous chapter, the presented method converges towards the analytical solution with an increasing number of supporting points. For this analysis, idealized conditions such as the exact time discretization of the motor model and the assumption of a linear magnetic motor circuit were used. However, the assumption of linear magnetization does not hold for NM-PMSMs. In addition, due to changes in speed or currents the motor model has to be discretized online in each sampling step. Hence, a time-consuming exact discretization with the matrix exponential is disadvantageous and the approximation by the forward Euler method should be the preferred choice.

Hence, the influences of the nonlinear magnetization as well as the approximation by the FE method on the solution accuracy need to be investigated. Here, the current trajectory during six-step operation of a NM-PMSM at rated operation

TABLE 2. NM-PMSM Model & LUT Parameters

PMSM	Brusa HSM16.17.12-C01	
Nominal power ($m = 1$)	P_{mech}	61 kW
Nominal speed ($m = 1$)	n_{mech}	4300 min^{-1}
Maximum speed	$n_{\mathrm{mech,max}}$	11 000 min^{-1}
Nominal torque	T_{nom}	136 Nm
Pole pair number	p	3
DC-link voltage	u_{DC}	300 V
Nominal current	I	177 A
Stator resistance	R_{s}	18 mΩ
Permanent magnet flux	ψ_{p}	68 mVs
LUT Parameters for $\boldsymbol{\psi}_{\mathrm{dq}}(\boldsymbol{i}_{\mathrm{dq}})$ and $\boldsymbol{L}_{\mathrm{dq},\Delta}(\boldsymbol{i}_{\mathrm{dq}})$		
Grid resolution d-direction	Δi_{d}	10 A
Grid resolution q-direction	Δi_{q}	10 A
Interpolation method	Linear	

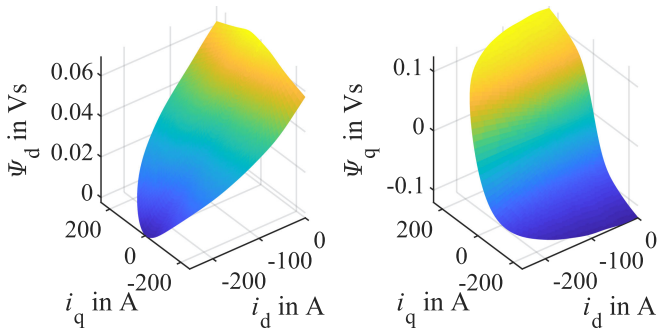

FIGURE 11. Flux maps of the utilized NM-PMSM motor model

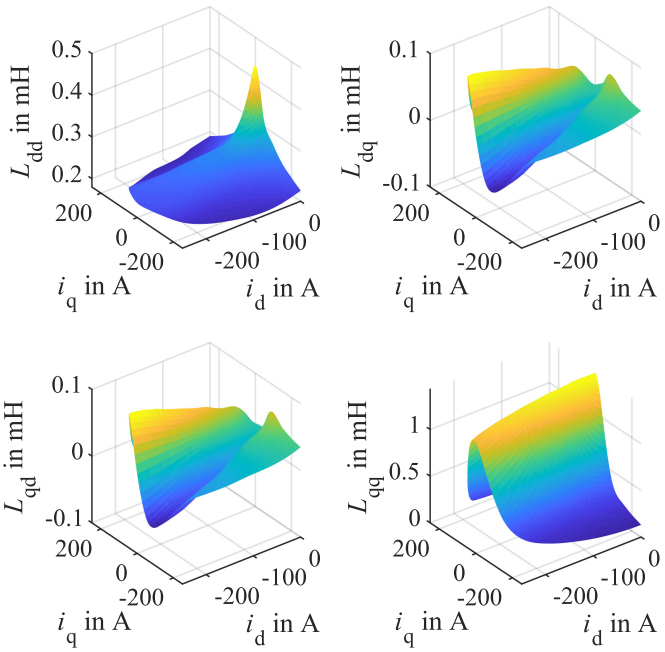

FIGURE 12. Differential inductances of the utilized NM-PMSM motor model

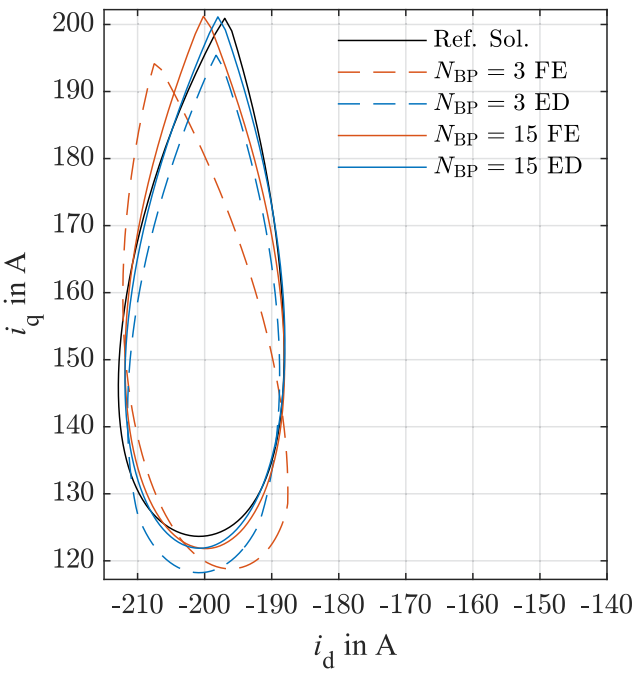

FIGURE 13. Solution trajectories for $m = 1$ at $\overline{i^*_{\mathrm{dq}}} = [-200 \quad 150]^{\mathrm{T}}$A for a NM-PMSM model using the ED and FE discretization method

is studied, since the largest harmonics occur here due to the comparably low speed and low differential inductances as a result of (cross-)saturation effects. The parameters of the investigated NM-PMSMas well as the hyperparameters of the LUTs characterizing the magnetic behavior are listed in Table 2. The flux linkages and differential inductances are shown in Fig. 11 and 12. Compared to the LM-PMSM model no analytical reference solution of the BVP exists due to the nonlinear magnetization. In the case of the NM-PMSM model the reference solution of the BVP was determined by a time domain simulation. In Fig. 13 the reference solution as well as the numerical solution of the BVP for different numbers of supporting points for the FE and the ED method were depicted for rated operation of the modeled PMSM. The mean error for both discretization methods as a function of the number of supporting points can be seen in Fig 14. It is revealed, that the solution of the FE method for an increasing number of supporting points comes close to the solution of the ED method. This occurs due to the fact, that the discretization step size is indirectly proportional to the number of supporting points and, therefore, the discretization error becomes smaller and smaller by the FE method. Although the mean error is reduced for an increasing number of supporting points, a residual error remains. This residual error can be explained by the nonlinear magnetization. Due to the large area of the current trajectories, model deviations occur due to the linearization, which are resulting in a remaining mean error.

This error disappears by repeatedly solving the linear system of equations (15). In each iteration the system matrices $\boldsymbol{\Phi}_n$, $\boldsymbol{H}_n$, $\boldsymbol{\Xi}_n$ in each line n have to be calculated using the

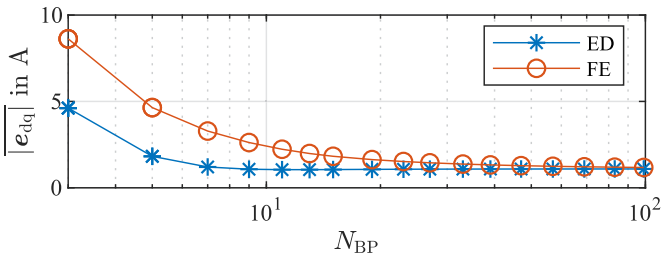

FIGURE 14. Mean error for $m = 1$ at $\overline{i^*_{dq}} = [-200 \quad 150]^T$A for a NM-PMSM model using the ED and FE discretization method

solution of the previous iteration $\boldsymbol{i}^*_{\mathrm{dq}|\mathrm{n}}$. However, the matrix $\boldsymbol{M}$ has to be inverted and the system matrices have to be calculated n-times using LUTs and then discretized in every iteration, this method is not pursued further because of the high computational load. As it will be discussed later, the remaining systematic model error is in such a small range, that overmodulation including six-step can be still achieved.

F. ENSURING SIX-STEP OPERATION

As seen in the previous section, even with exact knowledge of the motor parameters, errors in the solution of the BVP can occur due to a finite number of supporting points, the choice of the discretization method and the linearization of the magnetic motor model. In addition to these systematic errors, the solution of the BVP would also deviate from the PMSM's current trajectories due to inaccurate motor parameters based on various influences such as temperature, aging and further not modeled parasitic effects such as slot harmonics or the non-ideal inverter switching behavior.

When the trajectory of the HRG in steady state during six-step operation differs from the current trajectory of the PMSM, the CCS-MPCC tries to follow the current trajectory of the HRG through additional switching commands. Due to these additional switching commands the six-step operation cannot be realized by the CCS-MPC. However, two methods can be used to achieve six-step operation despite errors in the calculation of the BVP.

The first method is linked to the modulator and suppresses small corrections of the CCS-MPCC only during six-step operation by eliminating switching pulses shorter than a certain threshold $\mathrm{T_c}$. The second method concerns the HRG and the CCS-MPCC. Here, the matrix $\boldsymbol{R}$ in the optimization problem (6) weights the deviation between the optimization variable $\boldsymbol{u}_{\mathrm{dq}}[k]$ and the voltage of the HRG $\boldsymbol{u}^*_{\mathrm{dq}}[k]$. This matrix is chosen to $\alpha \boldsymbol{I}_2$. The larger α is selected, the closer $\boldsymbol{u}_{\mathrm{dq}}[k]$ moves to $\boldsymbol{u}^*_{\mathrm{dq}}[k]$, which reduces the voltage corrections due to deviations in the calculation of the reference trajectory. However, when the actual current is within the voltage limit of the linear modulation region, α is set to zero. A combination of both methods is useful here and ensures six-step operation at the voltage limit.

TABLE 3. Inverter, CCS-MPCC, PI-FOC, and HRG Parameters of the Simulative Test Setup

Inverter		
Switching frequency	f_{s}	10 kHz
Pulse clipping time at six-step operation	$\mathrm{T_c}$	10 µs
CCS-MPCC		
Controller cycle time	$\mathrm{T_s}$	50 µs
MPC prediction horizon	N	1
State weighting matrix	$\boldsymbol{Q}$	$\boldsymbol{I}_2\mathrm{A}^{-2}$
Input weighting matrix	$\boldsymbol{R}$	$0.01\boldsymbol{I}_2\mathrm{V}^{-2}$
PI-FOC		
Controller cycle time	$\mathrm{T_s}$	50 µs
Controller type	Decoupled PI controller	
Controller design	Magnitude optimum	
Dynamic overmodulation scheme	Minimum distance error [41]	
Anti-reset windup method	Back-calculation [42]	
HRG		
Number of supporting points	N_{BP}	5
Discretization scheme	ED	

IV. SIMULATIVE INVESTIGATION

On the basis of a simulation, the interaction of the HRG with the CCS-MPCC in a closed control loop is investigated. In order to verify whether the HRG can only be applied in combination with a CCS-MPCC, the CCS-MPCC is replaced by the PI-FOC in a further simulative investigation. Afterwards the simulation results are compared. The LM-PMSM motor model characterized by Table 1 is used for this study. Based on a torque step response following the MTPC strategy, the transient and steady-state behavior of the proposed method is analyzed for different constant velocities, which leads to different modulation indices.

A. CCS-MPCC

The inverter, CCS-MPCC, and HRG parameters are listed in Table 3. To avoid increasing the computational load, a prediction horizon of $N = 1$ was chosen, since an enlarged prediction horizon not only increases the complexity of the CCS-MPCC problem, but also that of the HRG since N future variable supporting points have to be added for the VSP method. In Fig. 15 the end of the linear modulation index $m = 0.907$ is reached at a speed of $2325\mathrm{min}^{-1}$ for the rated torque. Since the current controller does not operate at the voltage limit during steady-state, the current as well as the torque and voltage trajectories of the HRG are constants, whereby only torque and current harmonics occur due to the switching of the inverter. When the speed is increased further, the overmodulation region is entered and additional harmonics appear due to the voltage constraints in the current and voltage reference trajectories of the HRG, see Fig. 16. By following the current reference trajectory, a commanded voltage $\boldsymbol{u}_{\mathrm{dq}}$ is generated by the CCS-MPCC, which is close to the voltage trajectory $\boldsymbol{u}^*_{\mathrm{dq}}$ of the HRG. At a speed of $2570\mathrm{min}^{-1}$ the six-step operation must be applied to achieve the rated operating point. For this condition, the CCS-MPCC with and without the HRG is compared in Fig. 17. The elementary vectors $s_{\mathrm{n}} = \{1, 8\}$ are defined as in Fig. 1. Without a HRG the CCS-MPCC cannot maintain the operating point and switches back and forth between elementary vectors, see Fig. 17. In contrast, the

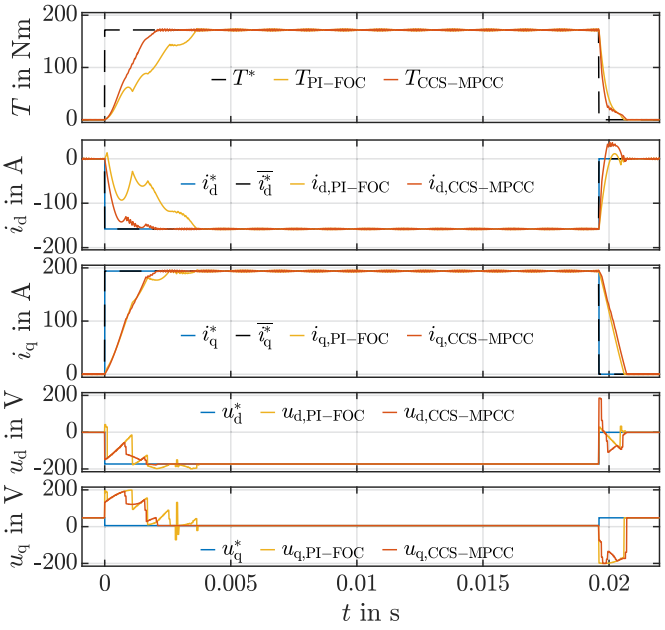

FIGURE 15. Torque step response to the rated torque following the MTPC strategy at a speed of 2325min^{-1} leading to a modulation index of $m = 0.907$

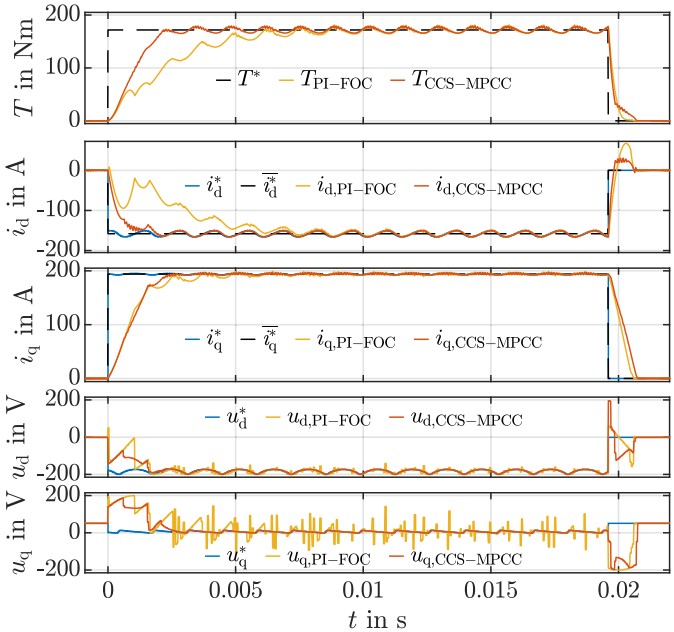

FIGURE 16. Torque step response to the rated torque following the MTPC strategy at a speed of 2461min^{-1} leading to a modulation index of $m = 0.959$

CCS-MPCC with the proposed HRG reaches the operating point and the six-step operation is realized, which minimizes the switching frequency and switching losses of the inverter.

B. PI-FOC

The parameters of the decoupled PI-FOC current controllers are listed in Table 3. For a successful application of the PI-FOC in combination with the HRG in the overmodulation

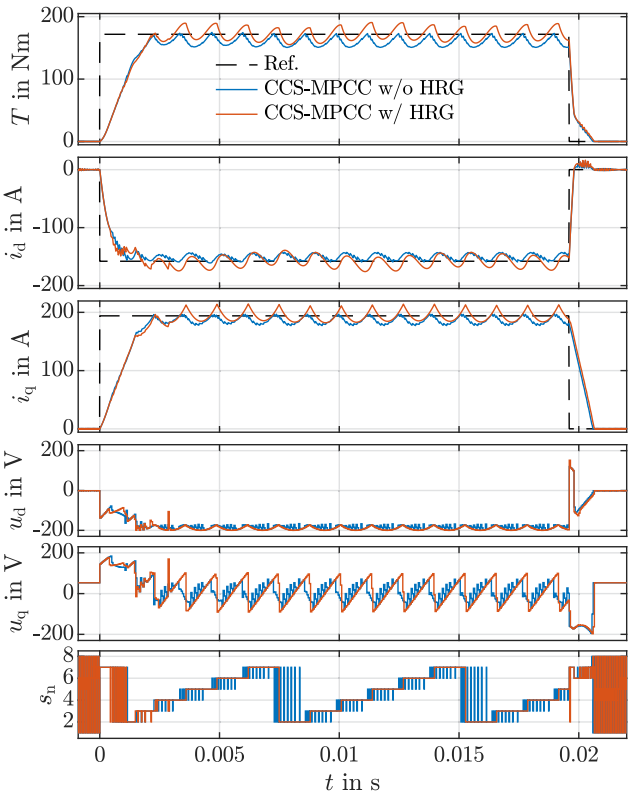

FIGURE 17. Torque step response to the rated torque following the MTPC strategy at the nominal speed of 2570min^{-1} for the CCS-MPCC with and without HRG

region including six-step operation, the following issues have to be considered:

1) Since the PI-FOC operates mainly at the voltage limit, it is essential to apply an anti-reset windup (ARW) strategy.
2) As for the CCS-MPCC, the compensation of the computation time must be performed using a one-step prediction with model (4) and cannot be accomplished by a forward rotating of state and output variables as it is usually done for PI-FOC.
3) On the one hand the CCS-MPCC can not choose infeasible voltages because of the inequality constraint (6b). The PI-FOC, on the other hand, can request infeasible voltages, which must be limited with a dynamic overmodulation scheme. Here, compared to the minimum phase error method [41] as dynamic overmodulation scheme, it has been shown that the minimum distance error method can achieve six-step operation.

As expected, the application of a CCS-MPCC can significantly improve the dynamic behavior compared to the PI-FOC, see Figs. 15–18 . At the end of the linear modulation region (m = 0.907), the steady-state behavior of the PI-FOC and the CCS-MPCC is identical, cf. Fig. 15. In the overmodulation region the current controller must track the time-varying current reference, as shown in Fig. 16. Here, a distortion of the voltage trajectories of the PI-FOC can be observed, which leads to additional current distortion and a suboptimal

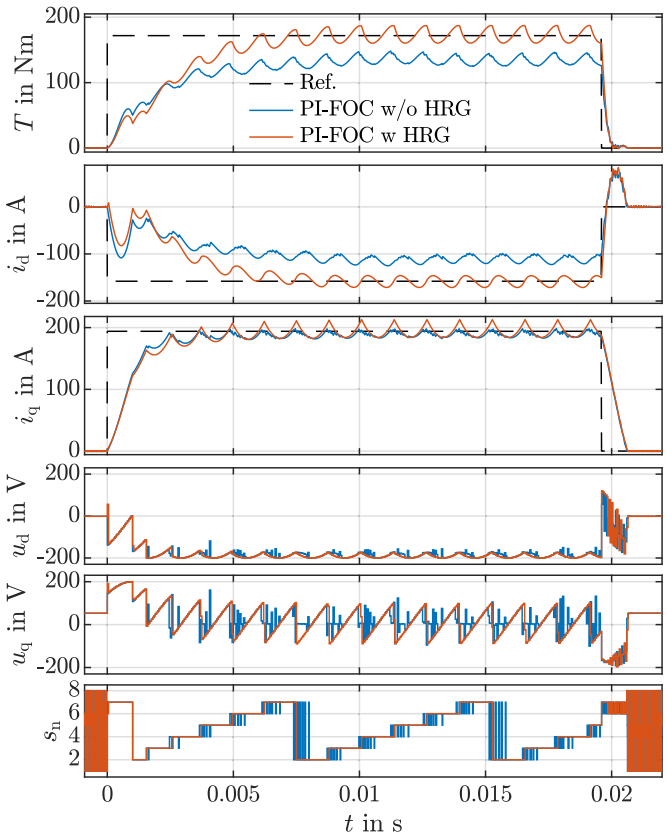

FIGURE 18. Torque step response to the rated torque following the MTPC strategy at the nominal speed of 2570min^{-1} for the PI-FOC with and without HRG

behavior. By applying the HRG to the PI-FOC, the behavior in the overmodulation region can be significantly improved so that six-step operation can also be achieved, cf. Fig. 18.

It can thus be seen that it is possible in principle to use the HRG approach to achieve overmodulation including six-step even with a simple PI-FOC current controller. This extends the range of applications of the presented HRG methodology. However, since the dynamic performance of the CCS-MPCC is significantly better and it can also be more elegantly combined with the HRG in terms of interfaces, only the CCS-MPPC in combination with the HRG will be investigated in the following experimental study.

V. EXPERIMENTAL INVESTIGATION

A. TEST SETUP

All following experimental results have been obtained on a laboratory test bench, see Fig. 19. The electrical drive system under test is a highly utilized interior permament magnet synchronous motor (Brusa: HSM1-6.17.12-C01) for automotive applications and a 2-level IGBT inverter (Semikron: 3×SKiiP 1242GB120-4D). The parameters and flux linkages as well as the differential inductances can be seen in Table 2, Fig. 11, and Fig. 12. As load motor, a speed-controlled induction machine (Schorch: LU8250M-AZ83Z-Z) is mechanically coupled with the test motor. The test bench is further equipped with a

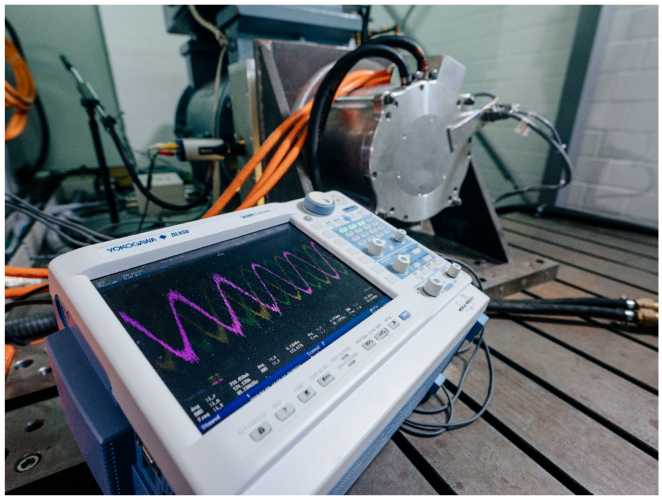

FIGURE 19. Test bench with the investigated PMSM in the background

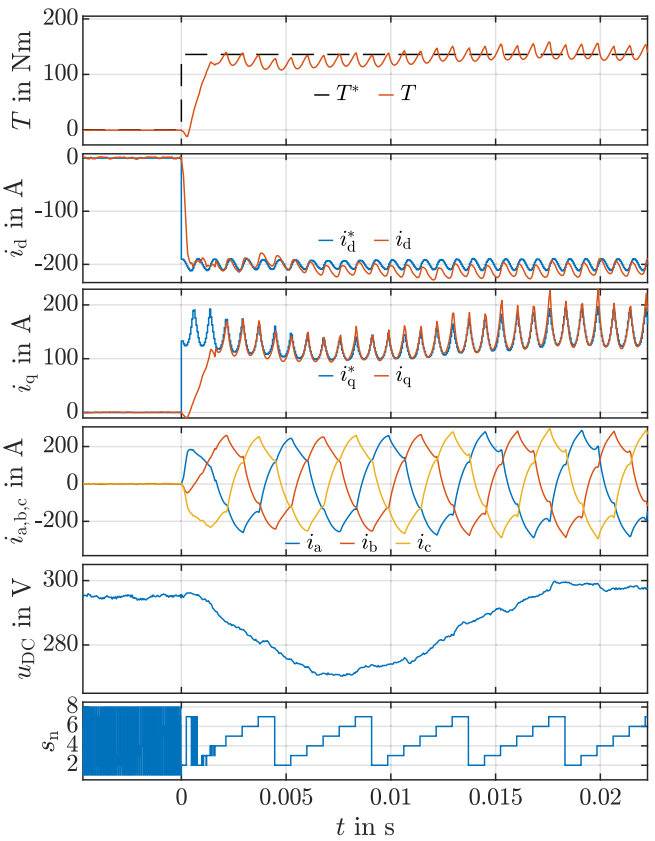

FIGURE 20. Torque step response to the rated torque following the MTPC strategy at nominal speed of 4300min^{-1}

dSPACE DS1006MC rapid-control-prototyping system. All measurements have been obtained by the dSPACE analog-digital-converters, which have been synchronized with the control task. The most important inverter, control, and test bench parameters are listed in Table 4. The mean turnaround time for the control framework in the linear modulation region was $32,8\mu$s with a standard deviation of $0,48\mu$s. In the overmodulation region, when the HRG is activated, the

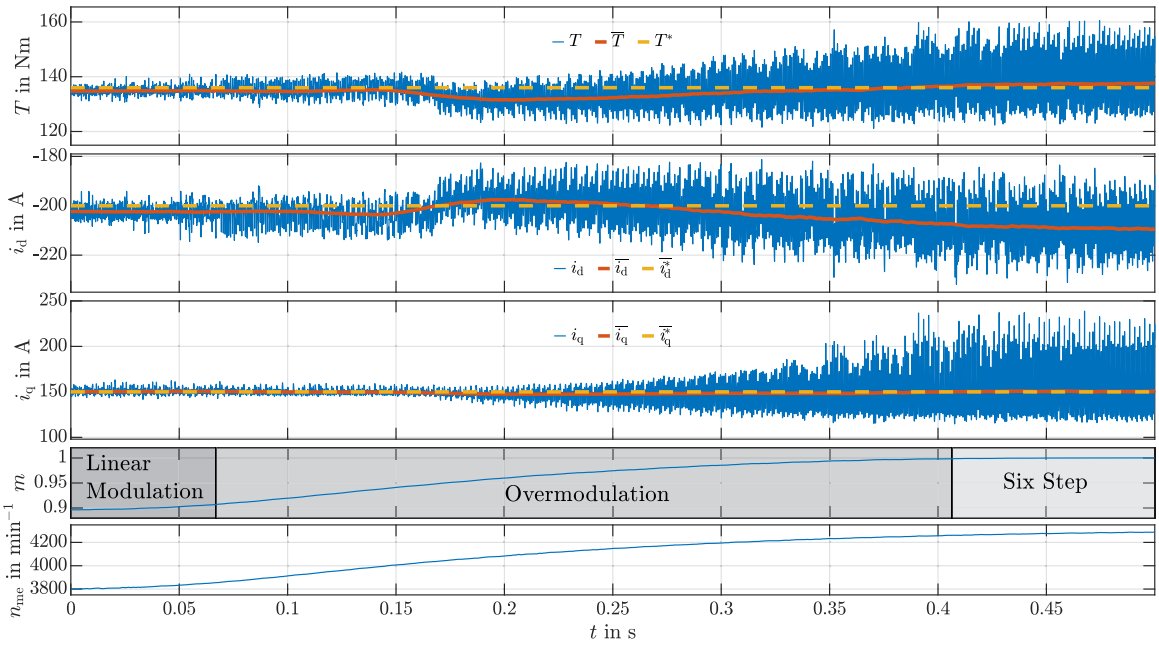

FIGURE 21. Speed transient from 3800min^{-1} to 4300min^{-1} at rated torque following the MTPC strategy, which leads to the rated current operation point $i_{dq} = \left[-200\text{A} \quad 150\text{A}\right]^{\mathsf{T}}$

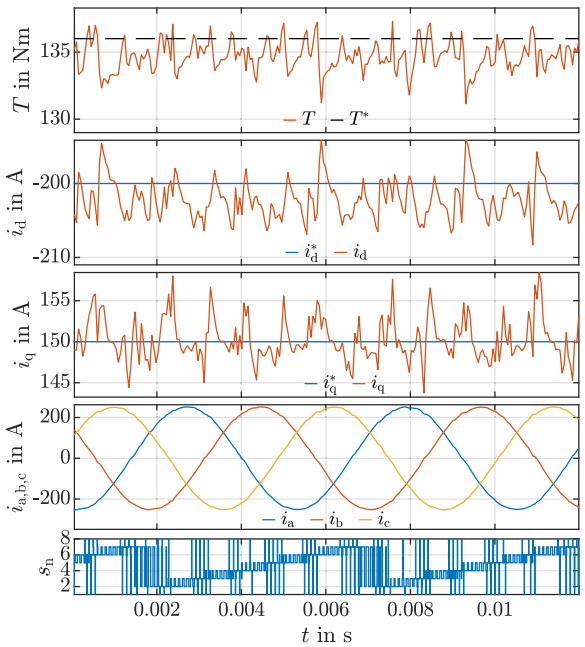

FIGURE 22. Zoom into previous Fig. 21 to highlight the torque as well as current trajectories and switching pattern nearby the end of the linear modulation region with $m = 0.89$ at rated torque following the MTPC strategy

TABLE 4. DC-Link, Inverter, Control, and Test Bench Parameters of the Experimental Test Setup

DC-link		Gustav Klein
Typology		DC-converter
DC-link capacitance		29 mF
Rated power		200 kW
Inverter		3×SKiiP 1242GB120-4D
Typology		Voltage source inverter 2-level, IGBT
Pulse clipping time at six-step operation	T_c	10 µs
Switching frequency	f_s	10 kHz
Inverter interlocking time	T_i	3.3 µs
CCS-MPCC		
Controller cycle time	T_s	50 µs
MPC prediction horizon	N	1
State weighting matrix	$\boldsymbol{Q}$	$\boldsymbol{I}_2\text{A}^{-2}$
Input weighting matrix	$\boldsymbol{R}$	$0.1\boldsymbol{I}_2\text{V}^{-2}$
HRG		
Number of supporting Points	N_{BP}	5
Discretization scheme		Forward Euler method
Controller hardware		dSPACE
Processor board		DS1006MC, 4 cores, 2.8 GHz
Measurement devices		
Oscilloscope		Tektronix MSO58
Current probes (zero-flux transducers)		3×Yokogawa, 500 A, 2 MHz
Torque sensor		HBM, T10FS, 2 kN m

mean turnaround time was 39, 1μs with a standard deviation of 0, 45μs.

In order to prove the effectiveness and performance of the controller during steady-state and transient operation, several challenging experiments were carried out in the constant-torque and constant-power region. Since the discrete-time measurement samples are synchronized with the SVM, the current ripple induced by the switching of the inverter is not visible in the following figures. Furthermore, the torque, depicted in the following figures is not measured directly with the help of a torque sensor. Instead, the torque was estimated with LUTs of the flux linkages $\psi_{d,q}(i_d, i_q)$ using the following relationship

$$T = \frac{3}{2} p \left[\psi_d\left(i_d, i_q\right) i_q - \psi_q\left(i_d, i_q\right) i_d\right]. \tag{20}$$

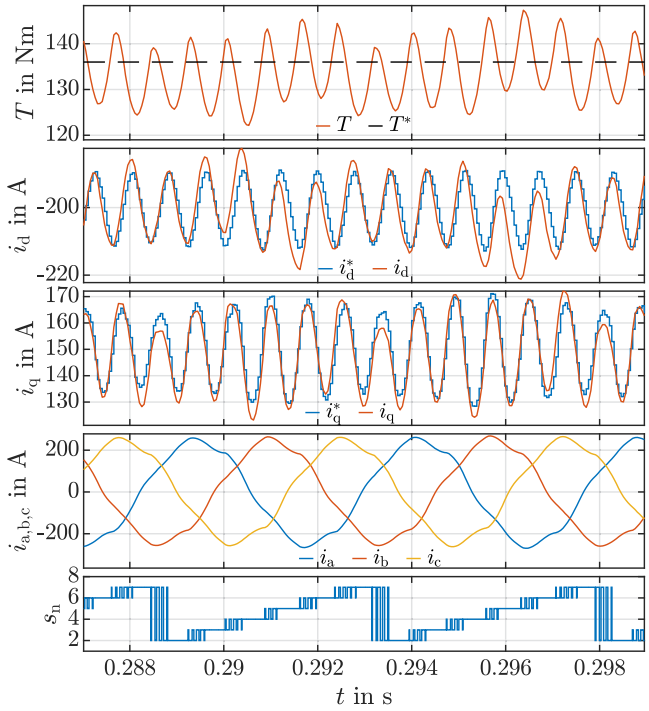

FIGURE 23. Zoom into previous Fig. 21 to highlight the torque as well as current trajectories and switching pattern in the overmodulation region with $m = 0.98$ at rated torque following the MTPC strategy

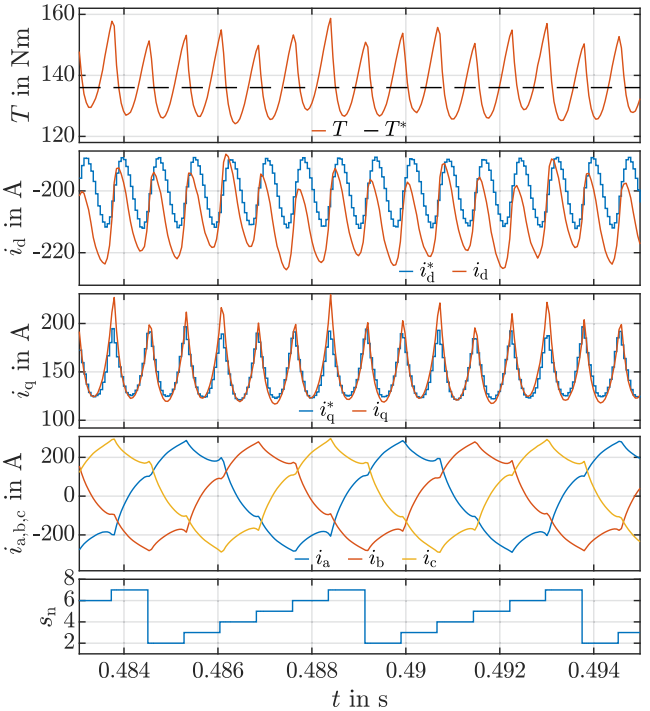

FIGURE 24. Zoom into previous Fig. 21 to highlight the six-step operation ($m = 1$) at rated torque following the MTPC strategy

The reliance on the estimation (20) rather than the direct shaft torque measurement can be legitimated for several reasons. On the one hand, highly dynamical experiments are investigated and, therefore, the moment of inertia of the rotor shaft as well as the limited bandwidth of the torque sensor distort the measurement. On the other hand, due to the finite stiffness of the connected motor shafts, mechanical resonance frequencies occur, which can be excited by the torque harmonics in the overmodulation region and, thus, further distort the torque measurement results.

B. CONSTANT-TORQUE REGION

In the constant-torque region, an operating point on the MTPC trajectory is usually selected to minimize copper losses. Hereby, the maximum torque is only constrained by the current limit. When the nominal speed is reached, the constant-torque region ends and the rated operating point is defined by the intersection of the current and voltage limit as well as the MTPC trajectory.

In order to investigate the transient behavior when the reference torque changes, the step response of the controlled system is shown in Fig. 20. The current controller reaches the reference trajectory within a remarkably short time and switches seamlessly to six-step operation. However, the rated operation point $\boldsymbol{i}_{\mathrm{dq}} = [-200\ \mathrm{A}\ \ 150\ \mathrm{A}]^{\mathrm{T}}$ cannot be reached until ≈ 0.02s. Due to the limited capacity of the DC-link capacitor and the finite settling time of the voltage controller

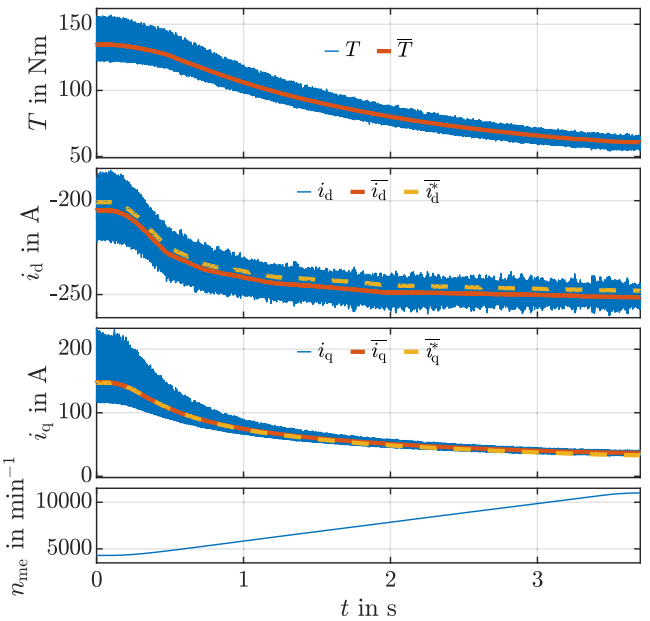

FIGURE 25. Speed transient from nominal to maximum speed while maximum torque operation is achieved

of the DC-link circuit, the current increase leads to a short-term reduction of the DC-link voltage. This short-term reduction leads to a contraction of the voltage limit, whereby an operating point with less flux linkage has to be selected by the higher-level open-loop torque controller. Nevertheless, the controller is able to maintain six-step operation and to

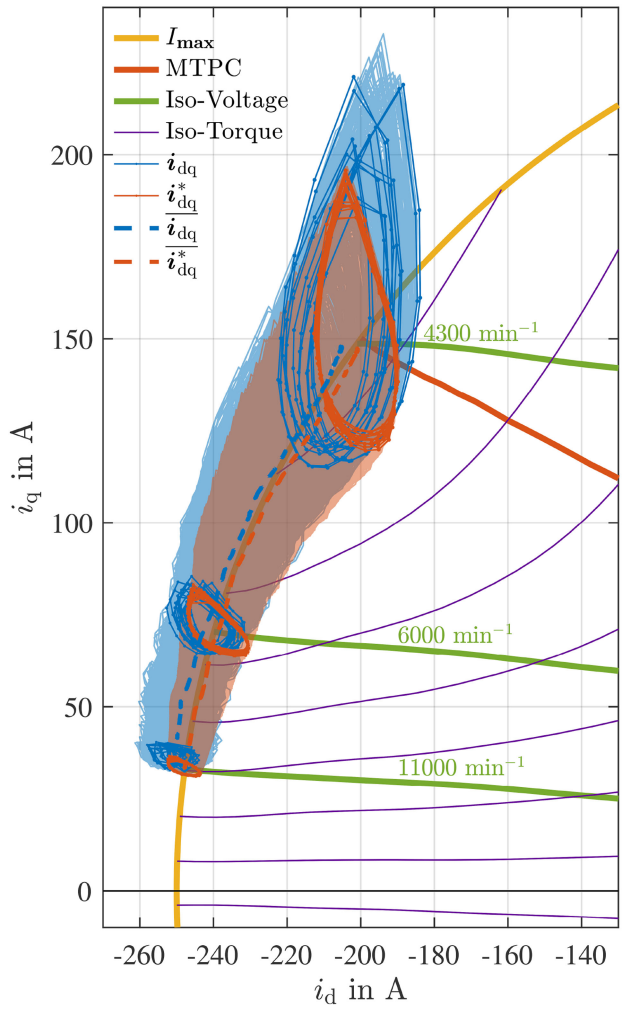

FIGURE 26. Current trajectories and operation-point-dependent as well as motor-characteristic loci during the speed transient from Fig. 25

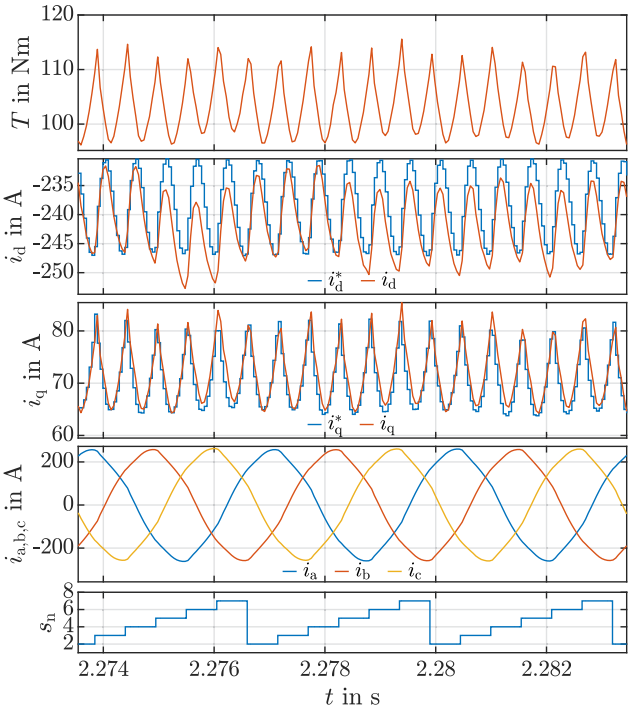

FIGURE 27. Torque as well as current trajectories and switching pattern at a speed of 6000min^{-1}

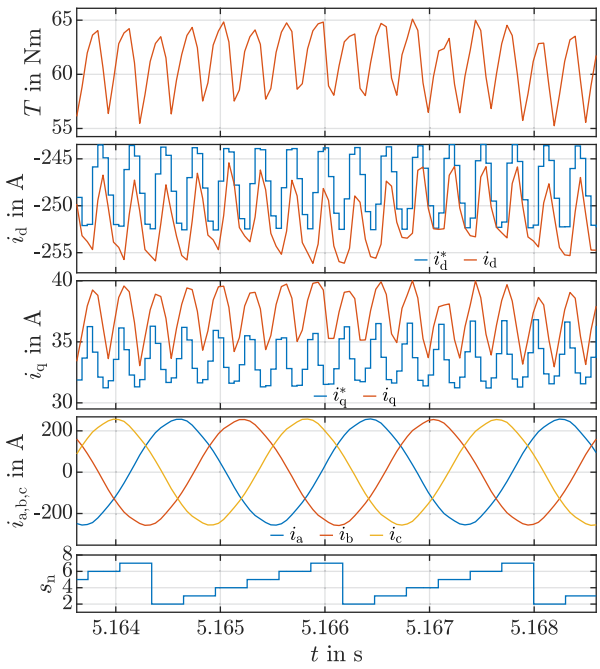

FIGURE 28. Torque as well as current trajectories and switching pattern at maximum speed (11 000min^{-1})

provide maximum torque in this challenging scenario. Operation feasibility at transiently varying DC voltages is an important feature of the presented methodology, as this problem is encountered in many industrial applications (e.g. automation and traction drives). To investigate the influence of a transient speed change on the controlled system, the speed was increased from 3800min^{-1} to 4300min^{-1} at the rated operation point, see Fig. 21. It should be mentioned again that the speed ramp is impressed for this test by the connected load machine, which is speed-controlled. Due to the changing speed, the voltage limit also changes, whereby the entire overmodulation region from linear modulation to six-step operation is covered. Here, a control deviation in the d-current and, therefore, also in the torque can be observed. This can be explained by a remaining model mismatch, the deviation of the solution of the BVP due to a finite number of supporting points, and the discretization method. To investigate the behavior of the controlled system for different modulation indices, some enlarged snapshots from Fig. 21 are depicted in Figs. 22–24. In the linear modulation region, as expected, the zero vectors are selected and there are no additional torque and phase current harmonics due to the voltage limit, see Fig. 22. With a modulation index of $m = 0.98$, the mean voltage vectors are located solely on the boundary of the voltage hexagon, which means that the zero voltage vectors are no longer selected. This creates additional torque and the phase current harmonics,

see Fig. 23. When the nominal speed is reached, the six-step operation must be applied to maintain the operating point, which leads to high phase current and torque harmonics, see Fig. 24.

C. CONSTANT-POWER REGION

The constant-power region is entered for speeds above the nominal speed. If maximum torque operation is required, the intersection of the voltage and current limit must be selected as the operating point. For PMSMs where the short-circuit point is within the current limit the intersection between the voltage limit and the MTPV trajectory must be selected as the operating point above a certain speed. Since the short-circuit point of the PMSM considered in this paper lies on the current limit, only operating points as intersection between voltage and current limits are used for the maximum torque operation in the constant-power region.

To analyze the performance of the controller in the constant-power region, the speed was increased from nominal to maximum speed during maximum torque operation, see Fig. 25 and Fig. 26. Only a minor control deviation can be detected. In order to generate the maximum torque, the voltage is utilized to its maximum, whereby the six-step operation is used continuously during the speed transient. For further investigations enlarged image details from Fig. 25 for different speeds are depicted in Fig. 27 and Fig. 28. Here, the reduction of phase current harmonics for higher speed despite six-step operation can be observed. This can be explained by two reasons: On the one hand, the voltage harmonics of the six-step operation have a decreasing impact on the currents for higher frequencies due to the low-pass characteristic of the stator winding system. On the other hand, the degree of saturation of the PMSM is lower for operating points at high speeds, which leads to larger differential inductance values, see Fig. 12, resulting in lower current harmonics. Despite the slight control deviation caused by the discussed systematic modeling errors, overmodulation operation including six-step can be maintained, which successfully enables the maximum power conversion of the drive system.

VI. CONCLUSION AND OUTLOOK

In this paper a model predictive control method for PMSMs with an integrated harmonic reference generator was presented and extensively investigated in simulations and experiments. By solving a linearly constrained quadratic optimization problem and adding a harmonic component to the reference current trajectories, the inverter can be fully utilized during transient and stationary operation. The manipulated reference current is calculated by the numerical solution of a boundary value problem, which enables overmodulation including six-step at the voltage limit. The presented control framework allows for both fast dynamic torque response during transients and maximum utilization of the drive system in the entire operating range without switching between different control strategies.

Since the presented solution approach requires an accurate drive model, online identification [43] or disturbance observer methods [44] will be integrated into the control framework to eliminate the found minor steady-state control error during future investigations.Moreover, the suitability of the presented HRG for FCS-MPC methods must be studied. In addition, it could also be demonstrated that overmodulation including six-step could be achieved for simple linear field-oriented current controllers by means of the presented reference generator, although this comes at the cost of reduced control dynamics compared to the model-predictive control approach. Furthermore, the applicability of the proposed method for other motor types, e.g. induction and synchronous reluctance machines, needs to be investigated.

REFERENCES

[1] R. Monajemy and R. Krishnan, "Performance comparison for six-step voltage and constant back EMF control strategies for PMSM," in *Proc. IEEE Ind. Appl. Conf.*, 1999, pp. 165–172.

[2] T. Schoenen, A. Krings, D. van Treek, and R. W. De Doncker, "Maximum DC-link voltage utilization for optimal operation of IPMSM," in *Proc. IEEE Int. Elect. Mach. Drives Conf.*, 2009, pp. 1547–1550.

[3] J. Holtz, "Advanced PWM and predictive control-an overview," *IEEE Trans. Ind. Electron.*, vol. 63, no. 6, pp. 3837–3844, Jun. 2016.

[4] O. Wallscheid, M. S. Shafiq, and J. Böcker, "Stator flux-based field-oriented position-sensorless control of permanent magnet synchronous motors with limited parameter knowledge," in *Proc. IEEE 28th Int. Symp. Ind. Electron.*, 2019, pp. 402–407.

[5] T. Huber, W. Peters, and J. Böcker, "Voltage controller for flux weakening operation of interior permanent magnet synchronous motor in automotive traction applications," in *Proc. IEEE Int. Electric Mach. Drives Conf.*, 2015, pp. 1078–1083.

[6] S.-M. Kim and S.-K. Sul, "Speed control of interior permanent magnet synchronous motor drive for flux weakening operation," in *Proc. IEEE Conf. Rec. Ind. Appl. Conf. 30th IAS Annu. Meeting*, 1995, pp. 216–221.

[7] N. Bedetti, S. Calligaro, and R. Petrella, "Analytical design and autotuning of adaptive flux-weakening voltage regulation loop in IPMSM drives with accurate torque regulation," *IEEE Trans. Ind. Appl.*, vol. 56, no. 1, pp. 301–313, Jan./Feb. 2020.

[8] A. M. Khambadkone and J. Holtz, "Compensated synchronous pi current controller in overmodulation range and six-step operation of space-vector-modulation-based vector-controlled drives," *IEEE Trans. Ind. Electron.*, vol. 49, no. 3, pp. 574–580, Jun. 2002.

[9] H. Nakai, H. Ohtani, and Y. Inaguma, "Novel torque control technique for high efficiency / high power interior permanent magnet synchronous motors," in *RD Rev. Toyota CRDL*, vol. 40, no. 2, pp. 44–49, 2005.

[10] S. Lerdudomsak, S. Doki, and S. Okuma, "A novel current control system for PMSM considering effects from inverter in overmodulation range," in *Proc. 7th Int. Conf. Power Electron. Drive Syst.*, 2007, pp. 794–800.

[11] S. Lerdudomsak, S. Doki, and S. Okuma, "Harmonic currents estimation and compensation for current control system of PMSM in overmodulation range -analysis for robustness to parameter variations," in *Proc. 34th Annu. Conf. IEEE Ind. Electron.*, 2008, pp. 1216–1221.

[12] K. Kondou and S. Doki, "A study on the application of the PMSM vector control system for high speed motor in inverter overmodulation range," in *Proc. IEEE Veh. Power Propulsion Conf.*, 2014, pp. 1–6.

[13] Y. Kwon, S. Kim, and S. Sul, "Six-step operation of PMSM with instantaneous current control," *IEEE Trans. Ind. Appl.*, vol. 50, no. 4, pp. 2614–2625, Jul.-Aug. 2014.

[14] S. Bolognani and M. Zigliotto, "Space vector fourier analysis of SVM inverters in the overmodulation range," in *Proc. Int. Conf. Power Electron., Drives Energy Syst. Ind. Growth*, 1996, pp. 319–324.

[15] P. Karamanakos and T. Geyer, "Guidelines for the design of finite control set model predictive controllers," *IEEE Trans. Power Electron.*, vol. 35, no. 7, pp. 7434–7450, Jul. 2020.

[16] J. Ishida, S. Doki, and S. Okuma, "Fast torque control system of PMSM based on model predictive control considering overmodulation region," in *Proc. Int. Power Electron. Conf. - ECCE ASIA* -Sapporo, Japan, 2010, pp. 1403–1406.

[17] M. Kadota, S. Lerdudomsak, S. Doki, and S. Okuma, "A novel current control system of IPMSM operating at high speed based on model predictive control," in *Proc. Power Convers. Conf. - Nagoya*, 2007, pp. 1315–1319.
[18] X. Wang, X. Fang, F. Lin, and Z. Yang, "Predictive current control of permanent-magnet synchronous motors for rail transit including quasi six-step operation," in *Proc. IEEE Transp. Electrific. Conf. Expo*, Asia-Pacific (ITEC Asia-Pacific), 2017, pp. 1–6.
[19] G. Pei, L. Li, X. Gao, J. Liu, and R. Kennel, "Predictive current trajectory control for PMSM at voltage limit," *IEEE Access*, vol. 8, pp. 1670–1679, 2020.
[20] C. F. Garcia, C. A. Silva, J. R. Rodriguez, P. Zanchetta, and S. A. Odhano, "Modulated model-predictive control with optimized over-modulation," *IEEE Trans. Emerg. Sel. Top. Power Electron.*, vol. 7, no. 1, pp. 404–413, Mar. 2019.
[21] A. Sarajian *et al.*, "Over-modulation methods for modulated model predictive control and space vector modulation," *IEEE Trans. Power Electron*., vol. 36, no. 4, pp. 4549–4559, Apr. 2021.
[22] F. Toso, P. G. Carlet, A. Favato, and S. Bolognani, "On-line continuous control set MPC for PMSM drives current loops at high sampling rate using qpOASES," in *Proc. IEEE Energy Convers. Congr. Expo.*, 2019, pp. 6615–6620.
[23] A. M. Hava, R. J. Kerkman, and T. A. Lipo, "Carrier-based PWM-VSI overmodulation strategies: Analysis, comparison, and design," *IEEE Trans. Power Electron.*, vol. 13, no. 4, pp. 674–689, Jul. 1998.
[24] J. Holtz, W. Lotzkat, and A. M. Khambadkone, "On continuous control of PWM inverters in the overmodulation range including the six-step mode," *IEEE Trans. Power Electron.*, vol. 8, no. 4, pp. 546–553, Oct. 1993.
[25] M. K. Modi and G. Narayanan, "Improved single-zone overmodulation algorithm for space vector modulated inverters," in *Proc. IEEE Int. Conf. Power Electron., Drives Energy Syst.*, 2014, pp. 1–6.
[26] D.-C. Lee and G.-M.Lee, "A novel overmodulation technique for space-vector PWM inverters," *IEEE Trans. Power Electron.*, vol. 13, no. 6, pp. 1144–1151, Nov. 1998.
[27] S. Bolognani and M. Zigliotto, "Novel digital continuous control of SVM inverters in the overmodulation range," *IEEE Trans. Ind. Appl.*, vol. 33, no. 2, pp. 525–530, Mar.-Apr. 1997.
[28] M. Depenbrock, "Direct self-control (DSC) of inverter-fed induction machine," *IEEE Trans. Power Electron.*, vol. 3, no. 4, pp. 420–429, Oct. 1988.
[29] K. Asano, Y. Inaguma, H. Ohtani, E. Sato, M. Okamura, and S. Sasaki, "High performance motor drive technologies for hybrid vehicles," in *Proc. Power Convers. Conf. - Nagoya*, 2007, pp. 1584–1589.
[30] H. Lee, J. Kim, J. Hong, and K. Nam, "Torque control for ipmsm in the high speed range based on voltage angle," in *Proc. IEEE Appl. Power Electron. Conf. Expo.* -, 2014, pp. 2500–2505.
[31] C. M. Hackl, J. Kullick, H. Eldeeb, and L. Horlbeck, "Analytical computation of the optimal reference currents for MTPC/MTPA, MTPV and MTPF operation of anisotropic synchronous machines considering stator resistance and mutual inductance," in *Proc. 19th Eur. Conf. Power Electron. Appl.*, 2017, pp. P.1–P.10.
[32] H. Eldeeb, C. M. Hackl, L. Horlbeck, and J. Kullick, "A unified theory for optimal feedforward torque control of anisotropic synchronous machines," *Int. J. Control*, vol. 91, no. 10, pp. 2273–2302, 2018.
[33] W. Peters, O. Wallscheid, and J. Böcker, "A precise open-loop torque control for an interior permanent magnet synchronous motor (IPMSM) considering iron losses," in *Proc. 38th Annu. Conf. IEEE Ind. Electron. Soc.*, 2012, pp. 2877–2882.
[34] W. Peters and J. Böcker, "Discrete-time design of adaptive current controller for interior permanent magnet synchronous motors (IPMSM) with high magnetic saturation," in *Proc. 39th Annu. Conf. IEEE Ind. Electron. Soc.*, 2013, pp. 6608–6613.
[35] A. Specht, S. Ober-Blöbaum, O. Wallscheid, C. Romaus, and J. Böcker, "Discrete-time model of an IPMSM based on variational integrators," in *Proc. IEEE Int. Electric Mach. Drives Conf.*, 2013, pp. 1411–1417.
[36] J. Böcker, "Discrete-time model of an induction motor," *Eur. Trans. Elect. Power*, vol. 1, no. 2, pp. 65–71, 1991.
[37] N. Khaled and B. Pattel, *Practical Design and Application of Model Predictive Control: MPC for MATLAB and Simulink Users*. London, U.K.: Butterworth-Heinemann, 2018.
[38] C. Schmid and L. Biegler, "Quadratic programming methods for reduced hessian SQP," *Comput. Chem. Eng.*, vol. 18, no. 9, pp. 817–832, 1994.
[39] P. Cortes, J. Rodriguez, C. Silva, and A. Flores, "Delay compensation in model predictive current control of a three-phase inverter," *IEEE Trans. Ind. Electron.*, vol. 59, no. 2, pp. 1323–1325, Feb. 2012.
[40] U. M. Ascher, R. M. M. Mattheij, and R. D. Russell, *Numerical Solution of Boundary Value Problems for Ordinary Differential Equations*. Philadelphia, PA, USA: SIAM, 1995.
[41] F. Briz, A. Diez, M. W. Degner and R. D. Lorenz, "Current and flux regulation in field-weakening operation of induction motors," *IEEE Trans. Ind. Appl.*, vol. 37, no. 1, pp. 42–50, Jan./Feb. 2001.
[42] K. J. Åström and T. Hägglund, *Advanced PID Control. ISA - the Instrumentation*, Research Triangle Park, NC 27709 Systems and Automation Society, 2005.
[43] A. Brosch, S. Hanke, O. Wallscheid, and J. Böcker, "Data-driven recursive least squares estimation for model predictive current control of permanent magnet synchronous motors," *IEEE Trans. Power Electron.*, vol. 36, no. 2, pp. 2179–2190, Feb. 2021.
[44] O. Wallscheid and E. F. B. Ngoumtsa, "Investigation of disturbance observers for model predictive current control in electric drives," *IEEE Trans. Power Electron.*, vol. 35, no. 12, pp. 13563–13572, Dec. 2020.

ANIAN BROSCH received the bachelor's and master's degrees in mechanical engineering from the Munich University of Applied Sciences, Munich, Germany, in 2016 and 2018, respectively. Since 2018, hehas been a Research Associate with the Department of Power Electronics and Electrical Drives, Paderborn University, Paderborn, Germany. His research focuses on identification and control of electrical drives, in particular model predictive control of highly utilized permanent magnet synchronous motors.

OLIVER WALLSCHEID (Member, IEEE) received the bachelor's and master's degree (hons) in industrial engineering and the Doctorate degree (hons) in electrical engineering from the Paderborn University, Paderborn, Germany, in 2010, 2012, and 2017, respectively. Since 2017, he has been a Senior Research Fellow with the Department of Power Electronics and Electrical Drives, Paderborn University. His research focuses on the modeling, experimental identification and intelligent control of highly utilized drives in automotive and automation applications.

JOACHIM BÖCKER (Senior Member, IEEE) received the Dipl.-Ing. and Dr.-Ing. degrees in electrical engineering from Berlin University of Technology, Berlin, Germany, in 1982 and 1988, respectively. He is currently a Professor and the Head of the Department of Power Electronics and Electrical Drives, Paderborn University, Germany. From 1988 to 2001, he was the Head of the control engineering team of the electrical drive systems laboratory, AEG and Daimler research. In 2001, he started his own business in the area of control engineering, electrical drives and power electronics. In 2003, he was appointed to the current professorship. His research interests include electrical drives, particularly for EVs and HEVs, energy management strategies for vehicles and smart grids, and converters for power supplies, EV chargers, and renewables.